Rheology Dependent on the Distance to the Propagating Thrust Tip—(Ultra-)Mylonites and Pseudotachylytes of the Silvretta Basal Thrust

Lisa M. Brückner[1] , **Claudia A. Trepmann[1], and Melanie Kaliwoda[1,2]**

[1]Department of Earth and Environmental Sciences, Ludwig-Maximilians-Universität München, Munich, Germany, [2]Mineralogische Staatssammlung München (MSM), Staatliche Naturwissenschaftliche Sammlungen Bayerns (SNSB), Munich, Germany

Abstract To evaluate how the presence of pseudotachylytes affects the strength of crustal rocks, deformed pseudotachylytes and their relationship with pristine pseudotachylytes at the base of the Silvretta nappe are analyzed. Pseudotachylytes formed associated with high-stress crystal plasticity ($\sigma_d > 400$ MPa), as indicated by twinned amphiboles in gneisses. Mylonitic quartz clasts enclosed within deformed pseudotachylytes and mylonitic vein-quartz, hosting folded pseudotachylyte injection veins, reflect creep at lower stresses (ca. 100 MPa) after seismic rupturing. Deformed pseudotachylytes can be crosscut by pristine pseudotachylytes, indicating a second, independent stage of coseismic rupturing after creep. The evidence of dynamic dislocation creep of quartz and the presence of stilpnomelane and epidote associated with all fault rocks indicate similar ambient greenschist facies conditions during all deformation stages. Whereas the intermediate stage of creep is interpreted to represent deformation at large distance to the propagating thrust tip, the pristine pseudotachylytes represent the last stage of rupturing eventually leading to nappe decoupling from its basement. Gneiss clasts in an ultramylonitic matrix (i.e., deformed pseudotachylyte) reveal that pseudotachylytes have a lower strength during creep in relation to the hosting gneisses. In contrast, during coseismic high-stress crystal plasticity, the coarse gneisses accumulate a higher amount of strain. This strength-relationship explains that only those rocks rupture, which have not been previously deformed before. The study demonstrates the importance of different strengths of crustal rocks at specific stress- and strain-rate conditions in dependence on the distance to the propagating fault tip.

1. Introduction

Pseudotachylytes are fault rocks resulting from the solidification of frictional melts formed along faults during seismic slip (slip rates of ~10^{-4}–10^{1} m/s, e.g., Cowan, 1999; Rowe & Griffith, 2015; Sibson, 1975). They are commonly described to crosscut each other and being themselves deformed (Bachmann et al., 2009; Campbell et al., 2020; Campbell & Menegon, 2019, 2022; Hawemann et al., 2018; Koch & Masch, 1992; Lin, 2008a, 2008b; Lin et al., 2003; Menegon et al., 2017; Moecher & Steltenpohl, 2009; Passchier, 1982; Pittarello et al., 2022; Price et al., 2012; Rowe et al., 2018; Sibson, 1980; Takagi et al., 2000; White, 1996, 2004). For large fault systems, incremental fault growth is predicted with multiple earthquake cycles (e.g., Cowie & Scholz, 1992; Dawers et al., 1993; Schlische et al., 1996; Stein et al., 1988; Walsh & Watterson, 1988). Therefore, crosscutting pseudotachylyte veins have been proposed to indicate repeated rupturing during successive seismic cycles (e.g., Koch & Masch, 1992; Swanson, 1992). The formation of pseudotachylytes and mylonites can take place under the same metamorphic conditions, as recorded by mutual overprinting relationships (Altenberger et al., 2011, 2013; Koch & Masch, 1992; Moecher & Steltenpohl, 2009; Pennacchioni & Cesare, 1997; Pittarello et al., 2012; White, 1996, 2004, 2012). As such, deformed pseudotachylytes, which predate and outlast mylonites, were interpreted as recurring earthquake cycles (Hawemann et al., 2018; Koch & Masch, 1992; Lin, 2008b; Moecher & Steltenpohl, 2009; Takagi et al., 2000). Complex networks of crosscutting pseudotachylytes can, however, also be generated by one single large rupturing event (Allen, 2005; Grocott, 1981; Rowe et al., 2018). During a single rupture, deformation mechanisms can vary (Kirkpatrick & Shipton, 2009) and several slip surfaces can be active in parallel (Heesakkers et al., 2011; Swanson, 2006), which can be reused in large earthquakes (Allen, 2005; Kirkpatrick & Shipton, 2009). Rowe et al. (2018) presented field observational criteria for branching and coalescing ruptures that generate complex pseudotachylyte networks formed in one single seismic event. At the basal thrust of the Preveli crystalline nappe on Crete, only one prominent and unique imprint of coseismic deformation

with the formation of pseudotachylytes at one specific location is described by Nüchter et al. (2013). These authors proposed a model of coseismic thrust fault propagation, in which dependent on the distance to the propagating fault tip, a characteristic sequence of deformation structures develops. With decreasing distances, ductile (e.g., kink bands) to brittle structures (quartz veins) and finally pseudotachylytes, as the last microstructural imprint recording earthquake rupturing, form. In this model, strain after the passage of the fault front is localized in the next rock increment, eventually causing the decoupling of the nappe from its original basement before subsequent transport over large horizontal distances onto a foreign tectonic unit. During nappe transport, low shear stresses are required, and further strain is localized in weak lithologies and areas of high pore fluid pressure (Bachmann et al., 2009; Cook & Aitken, 1976; Davis & Engelder, 1985; Davis et al., 1983; King Hubbert & Rubey, 1959; Koch & Masch, 1992; Laubscher, 1983; Rodgers et al., 1962). Passelègue et al. (2021) showed experimentally that pseudotachylytes are prone to deformation by diffusional creep and concluded that the rheology of pseudotachylytes can reduce the strength of the continental crust. In contrast, pseudotachylyte formation, which welds the fault plane, can prevent the occurrence of shear on the same slip surface and that subsequent failure arises at a new site (Mitchell et al., 2016; Proctor & Lockner, 2016).

The question, of whether fault rocks or their host rocks control the strength of the continental crust is related to the question of their relative strength (a) during coseismic high-stress plasticity and (b) during creep. In order to evaluate the deformation conditions, we use the microstructural record of the different Silvretta fault rocks (deformed and non-deformed, i.e., pristine pseudotachylytes, as well as (ultra-)mylonites). The implications for the strength of the various fault rocks during the different stages and the assignment of the recorded coseismic rupturing event(s) to the Alpine stages are discussed. For the purpose of this paper, we will use the term "mylonites" in the sense of localized high-strain zones, where quartz-rich layers deformed dominantly by dislocation creep developing a marked crystallographic preferred orientation (CPO) of dynamically recrystallized grains. We refer to "ultramylonite" for Silvretta fault rocks which are characterized by fine-grained polyphase layers containing less than 10% porphyroclasts (Passchier & Trouw, 2005), mostly comprised of quartz deformed by dislocation creep.

2. Geological Setting

The Silvretta crystalline in the central Alps (Figures 1a and 1b) represents one of the Upper Austroalpine basement nappes (Froitzheim et al., 1994; Schmid et al., 2004), which was decoupled from its original basement and thrusted over the Penninic units (Figure 1c) during the Alpine orogeny (Laubscher, 1983). The nappe, composed of Variscan paragneisses, orthogneisses and amphibolites, covers about 1,600 km^2 (Maggetti & Flisch, 1993; Masch, 1970; Thöni, 1981, 1988; Wenk, 1934). The original basement (Insubric crystalline) is suggested to have a similar composition as the Silvretta nappe (Schmutz, 1995). At the contact zone to the Penninic units of the Engadin Window, the metamorphic conditions during the Eo-Alpine at about 110 to 85 Ma are reported to have been in the range of 350–540°C and 300–400 MPa (Hurford et al., 1989; Maggetti & Flisch, 1993; Thöni, 1981).

The fault rocks of the Silvretta basal thrust comprise pseudotachylytes, mylonites, and ultramylonites described in detail by Masch (1970), Koch (1990), Koch and Masch (1992), and Schmutz (1995). The various fault rocks developed at lower greenschist facies conditions between 300 and 400°C, as indicated by their Alpine mineral paragenesis (Koch & Masch, 1992; Schmutz, 1995), which is consistent with the related quartz microfabrics in the hosting rocks (Bachmann et al., 2009; Trepmann et al., 2017). The Variscan foliation of the gneisses and mylonites is striking WE to NE with mostly shallow dip angles of 10°–30° (Hammer, 1914; Koch & Masch, 1992; Masch, 1970; Schmutz, 1995). Pseudotachylytes occur as concordant, discordant, branching dykes, and as breccias (Figure 2) (Masch, 1970; Schmutz, 1995). The occurrence of these fault rocks is related to the base of the thrust fault (Figures 1b and 1c). Pseudotachylytes are restricted to within 300 m above the base of the nappe in the hanging wall of the thrust and are most common at about 100–200 m above the thrust (Koch & Masch, 1992; Masch, 1970, 1974; Schmutz, 1995). At the northwestern border to the Engadine Window (Figures 1b and 1c), they can cover up to 40% of the outcrops (Bachmann et al., 2009). Given their association with the hanging wall of the thrust and the observation that no components of the Penninic units occur in the pseudotachylytes, as well as the absence of pseudotachylytes in the footwall of the thrust shows that they have formed during the initial nappe decoupling and before transport over the Penninic units (Koch, 1990; Koch & Masch, 1992; Laubscher, 1983; Schmutz, 1995). Based on detailed mesoscopic analyses of the structural inventory of the fault rocks and the orientation relationship between foliation, pseudotachylyte-bearing faults, and the thrust plane, Schmutz (1995) concluded, that the thrust fault plane was subsequently bent upon the formation of the Engadine Window. Isotopic investigations of pseudotachylytes reveal a formation in Late Cretaceous to Paleocene epochs (^{87}Rb/^{86}Sr whole rock about 75 Ma:
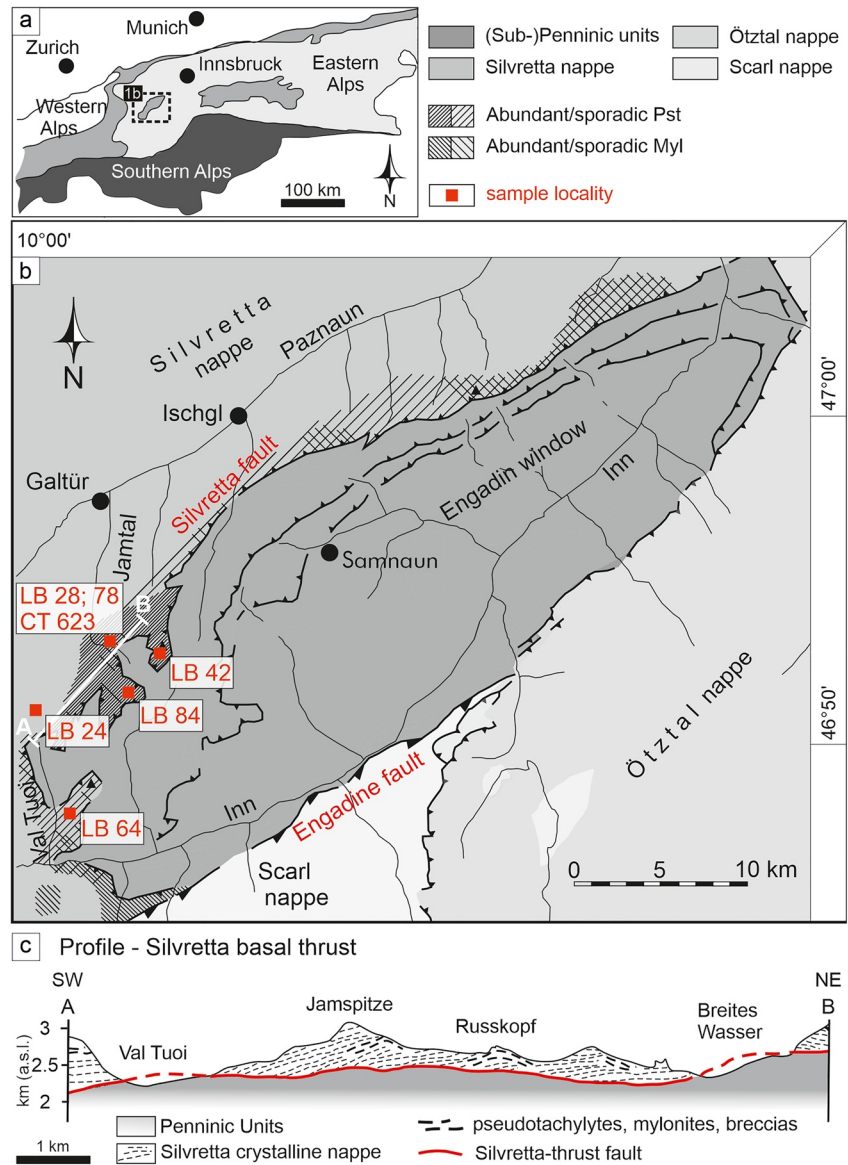
Figure 1. Geological overview of the Silvretta crystalline. (a, b) Schematic geological map of the study area within the central Alps and sample locations at the western contact of the Silvretta nappe to the Penninic units of the Engadine Window with the distribution of pseudotachylytes (pst) and mylonites (myl) (modified after Koch & Masch, 1992). (c) Schematic geological profile of the basal thrust fault along the AB profile line in (b) (modified after Schmutz, 1995).

Thöni, 1988; $^{40}Ar/^{39}Ar$ whole rock 62–78 Ma: Bachmann et al., 2009). Recently, Pittarello et al. (2022) suggested that only the relatively less common deformed pseudotachylytes were formed at greenschist facies conditions based on the presence of intergrown epidote-feldspar aggregates and that pristine pseudotachylytes formed at temperatures <250°C during subduction of the Penninic Unit in the Paleogene. The relationship between deformed pseudotachylytes, (ultra-)mylonites, and undeformed, that is, pristine pseudotachylytes of the basal Silvretta thrust, as well as their deformation conditions, are not well constrained so far. Here, we analyze the deformation record of the various Silvretta fault rocks, for evaluating the strength of the continental crust during the seismic cycle.

3. Methods

Deformed pseudotachylyte-bearing gneisses were sampled at the border of the Silvretta crystalline to the units of the Engadine Window in Austria (Figure 1b; LB24: 47°01′00″ N/10°28′00″ E; LB28: 46°53′23″ N/10°11′16″
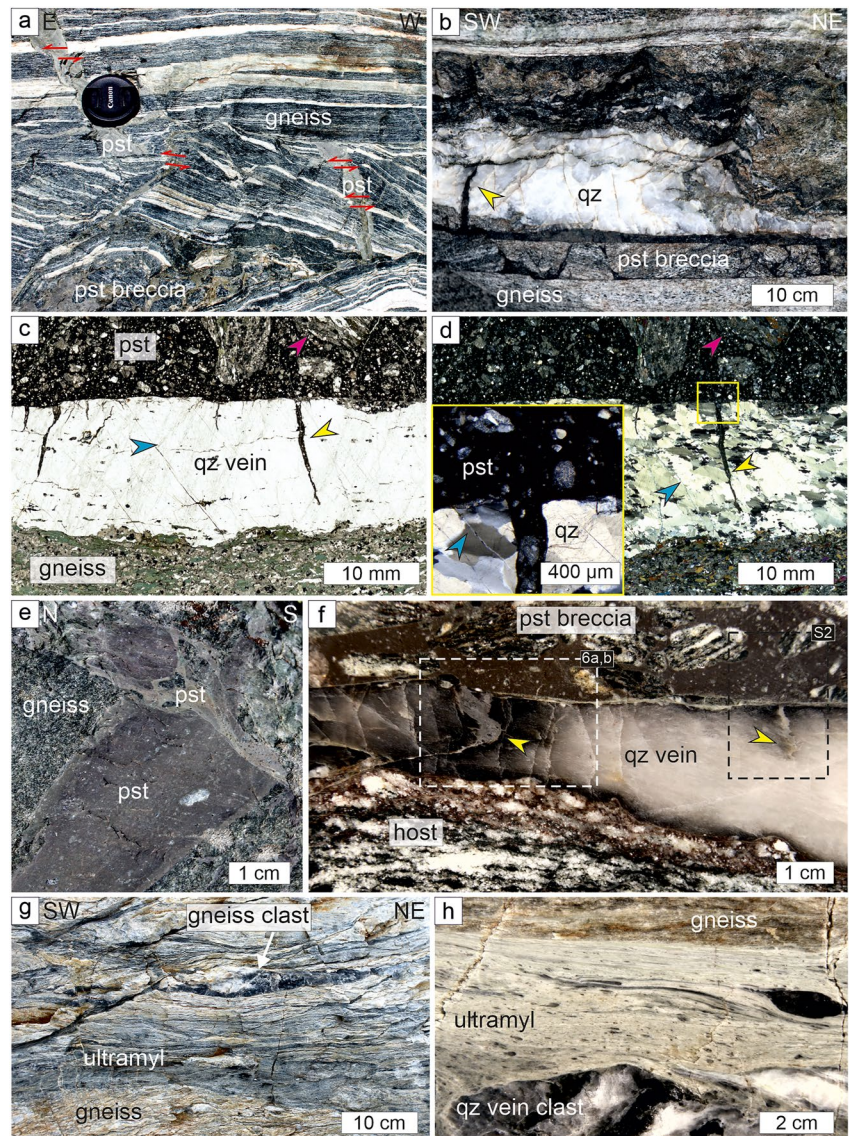
Figure 2. Fault rocks at the base of the Silvretta nappe. (a) Pseudotachylyte (pst) veins in brecciated amphibole-rich gneisses display offsets of several cm (red arrows). (b) Tabular pseudotachylyte breccia with injection vein into host quartz vein (qz, yellow arrow). (c, d) Polarized light micrograph, (d) is taken with crossed polarizers, showing straight injection veins (yellow arrows) from parent pseudotachylyte with a sharp boundary to coarse-grained quartz layer concordant to amphibole-rich gneiss, sample CT623c. Injection veins are affected by shear fractures (blue arrows). Close-up in (d) is showing sharp boundaries of injection veins to the coarse recrystallized quartz vein fabric. (e) Pseudotachylyte vein containing brecciated clasts of a primary pseudotachylyte. (f) Quartz layer concordant to foliated biotite-rich gneiss (host) with pseudotachylyte breccia containing large amphibole-gneiss clasts, sample LB78. Within the quartz layer, foliated and folded pseudotachylyte injection veins occur (yellow arrows). White and black rectangles display the position of Figures 6a and 6b, and Figure S2 in Supporting Information S1, respectively. (g, h) Ultramylonitic layers (ultramyl) within host gneisses that represent deformed pseudotachylyte, sample LB28. Note the low-spaced foliation, which is deflected around gneiss and vein-quartz clasts in (h).

E; LB42: 46°52′57″ N/10°12′57″ E; LB64: 46°48′03″ N/10°09′06″ E; LB78: 46°52′50″ N/10°10′18″ E; LB84: 46°51′39″ N/10°12′47″ E; CT623: 46°55′21″ N/10°10′30″ E). Thin sections with a thickness of ca. 30 μm were prepared perpendicular to the main foliation (Z) and parallel to the stretching lineation (X). The samples were investigated by polarized light microscopy and scanning electron microscopy (SEM) including electron backscattered diffraction (EBSD). We used the SU5000 Hitachi field emission microscope at the Department of Earth and Environmental Sciences, LMU Munich, equipped with an HKL Nordlys-Nano electron backscatter diffraction detector. For EBSD analysis, thin sections were polished with an alkaloid colloidal suspension

(Syton) for 1.5 hr. A pre-tilted sample holder with an angle of 70° relative to the horizontal, working distances of 15–25 mm, and an acceleration voltage of 20 kV was used. Data were acquired and processed with the Aztec 4.2 and CHANNEL 5 software of Oxford Instruments (Oxford Instruments, 2020), respectively. Automatic EBSD maps were measured with a step size of 0.8–1.3 μm. As a threshold for grain detection, a misorientation angle of 10° was applied. All pole figures are displayed as equal-angle stereographic projections of the lower hemisphere. The 2D orientation of the long grain axes (rose diagram) is displayed and analyzed with the Stereo32 software (Röller & Trepmann, 2003).

To confirm the presence of stilpnomelane, Raman spectroscopy was carried out by using a HORIBA JOBIN YVON XploRa ONE micro Raman spectroscope located at the Mineralogical State Collection Munich (Staatliche Naturwissenschaftliche Sammlungen Bayerns [SNSB]), using a 2ω-Nd:YAG laser with a wavelength of 532 nm in an attenuated mode of 25% laser power, that is, 2.5 mW on the sample surface. The hole and slit were set to 100 and 50 μm, respectively. For better spectral resolution, an 1,800 T grating was used and a 100 long working distance objective was employed. We used an acquisition time and accumulation time of 8 s and 2 runs, respectively. Wavelength calibration was performed with a pure Si wafer chip on the predominant 520 ± 1.5 cm^{-1} band. The accuracy of all Raman peak band positions is estimated at ± 1.5 cm^{-1} for subsequent measurements. Raman data were acquired and processed with the LabSpec 6.6.1 software of Horiba Scientific (Horiba Scientific, 2022). Furthermore, a stilpnomelane sample (#23472) from Wurlitz/Oberkotzau, Germany, provided by the Mineralogical State Collection Munich (SNSB), was used as a comparison standard for optimum stilpnomelane identification.

4. Results

4.1. Investigated Samples and Field Observations

The investigated pseudotachylyte-bearing Silvretta host rocks comprise foliated amphibole-rich gneisses (Figures 2a–2e) and biotite-rich gneisses (Figure 2f). The gneisses commonly show concordant quartz veins containing >95% quartz (Figures 2a–2d and 2f). The amphibole-rich gneisses comprise about 40%–60% amphibole, 20%–40% plagioclase, 10%–30% quartz, 0%–10% biotite, and 0%–5% white mica. Biotite gneisses comprise about 20%–30% quartz, 20%–30% biotite, 30%–40% feldspar, and 10%–15% green hornblende. Sphene, zircon, ilmenite, rutile, epidote, and stilpnomelane occur as accessory constituents in both gneisses.

Pseudotachylytes occur as complex vein networks within brecciated host gneisses, where the single veins are a few mm to dm in thickness (Figures 2a–2f). The main pseudotachylytic veins are commonly found subparallel or slightly oblique to the foliation of the host gneisses and concordant quartz veins, in which a few hundred μm to cm long and μm to mm wide injection veins at a high angle to the main pseudotachylyte can occur (Figures 2a–2d and 2f). Pseudotachylytes can crosscut other pseudotachylytes with offsets of a few hundred microns to several cm (Figure 2a). Angular (Figure 2a) and tabular breccias (Figures 2b and 2f), as defined by Rowe et al. (2018) are common. Less commonly, brecciated clasts of pseudotachylytes within pristine pseudotachylytic veins occur (Figure 2e). The injection veins are mostly straight (Figures 2a–2d) but can be affected by shear fractures within the host quartz (Figures 2c and 2d). The hosting quartz usually shows a coarse recrystallization fabric unrelated to the crosscutting straight injection veins (Figure 2d). In addition, folded injection veins can be found, which show a sharp contact with another pseudotachylyte that shows no field evidence of deformation (Figure 2f). Ultramylonites, which represent deformed pseudotachylytes (e.g., dynamic recrystallization of quartz, Koch & Masch, 1992), are characterized by a low-spaced foliation deflected around cm-sized gneiss- and vein-quartz clasts (Figures 2g and 2h).

The pseudotachylytes exhibit a fine-grained matrix with clasts of the host gneisses, several cm to dm in diameter (Figures 2c–2f). The strongly varying composition of the pseudotachylytes depends on the local host rock lithology (Koch & Masch, 1992; Schmutz, 1995). Within biotite-rich gneisses, pseudotachylytes often contain aggregates of intergrown epidote and feldspar, whether they are pristine (Figures 3a–3c) or deformed (Figures 3d–3f). In contrast, in the more common amphibole-rich gneisses these epidote-feldspar aggregates have not been observed. Pittarello et al. (2022) reported similar epidote aggregates in the Silvretta fault rocks and interpreted them to indicate greenschist facies conditions. Stilpnomelane is observed by polarized light microscopy and SEM as fine needles (width: ~1 μm; length: 30–100 μm) in both, pristine (Figures 3a and 3c), as well as deformed pseudotachylytes (Figures 3d and 3f), and within all types of Silvretta gneisses. The presence of stilpnomelane in the pristine and deformed pseudotachylytes has been confirmed by Raman spectroscopic investigations (Text
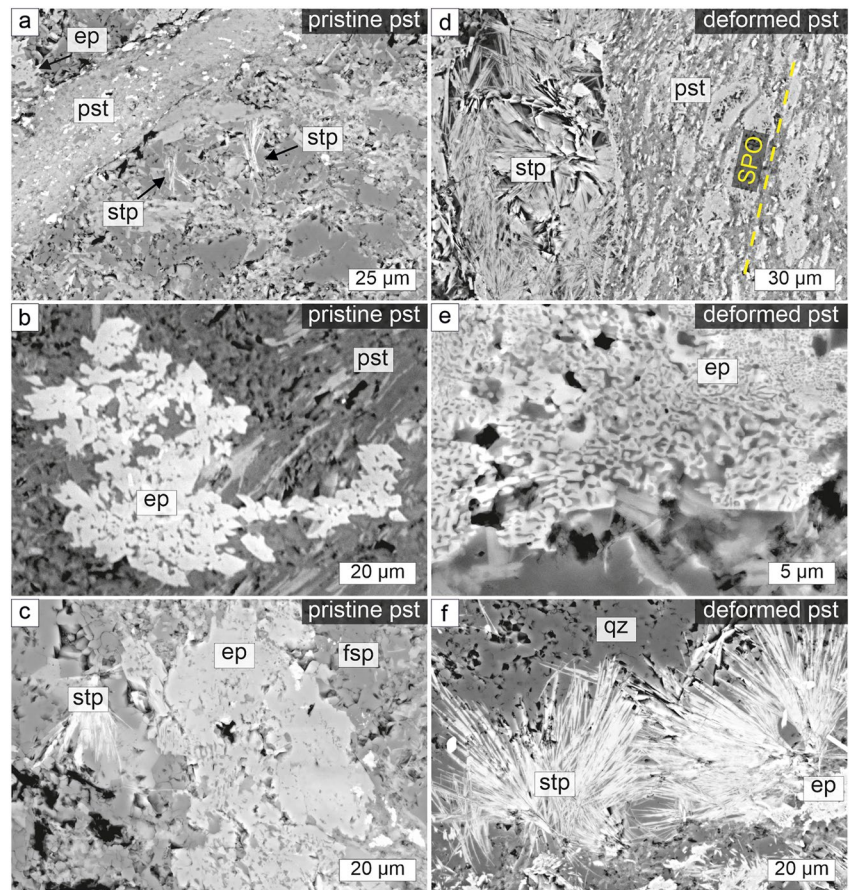
Figure 3. Backscattered electron (BSE) images of stilpnomelane and epidote within pristine (a–c) and deformed (d–f) pseudotachylytes. (a) Stilpnomelane (stp) and epidote (ep) associated with pristine pseudotachylyte (pst), sample LB64b. (b) Intergrown epidote-feldspar aggregate, sample LB84b. (c) Epidote and stilpnomelane aggregates embedded in a feldspar-rich (fsp) gneiss clast within pseudotachylyte, sample LB64b. (d) Stilpnomelane aggregates in contact with deformed pseudotachylyte showing a matrix with a shape preferred orientation (SPO, yellow dashed line), sample LB42b. (e) Epidote-feldspar intergrowth, sample LB78b. (f) Stilpnomelane together with epidote in a quartz-rich (qz) gneiss clast, sample LB42a.

S1 in Supporting Information S2 and Figure S1 in Supporting Information S1). Stilpnomelane has already been described by Koch and Masch (1992) to occur in all Silvretta fault rocks and is taken to indicate greenschist facies conditions. For a detailed field description and occurrence of the pseudotachylytes, the reader is referred to Koch and Masch (1992) and Schmutz (1995).

Most of the observed crosscutting relationships of pseudotachylytes fulfill the criteria of complex networks that can be generated within a single seismic event (e.g., angular breccias in Figure 2a and tabular breccias in Figure 2b, as defined by Rowe et al. (2018)). The relationship between deformed and pristine pseudotachylytes, as well as (ultra-)mylonites (Figures 2e–2h and 4a), however, cannot be revealed by field observations alone. Three representative samples that contain both, deformed and pristine pseudotachylytes from more than 80 analyzed pseudotachylyte-bearing gneisses, were chosen for detailed microstructural analysis (Figure 1b): (a) deformed pseudotachylytes (pst1) grading into ultramylonites, sample LB28 (Figures 2h, 4, and 5); (b) folded and foliated injections veins (pst1) in a foliated quartz vein crosscut by undeformed pristine pseudotachylytes (pst2, pst3), sample LB78 (Figures 2f and 6–8) and (c) brecciated pseudotachylytes, sample LB24 (Figures 2a, 2e, and 9).

4.2. Deformed Pseudotachylytes Grading Into Ultramylonites

The deformed pseudotachylytes are characterized by a well-developed foliation deflected around larger gneiss clasts (Figures 2g, 2h, and 4a). The matrix grains, as well as clasts, reveal an associated shape-preferred orientation
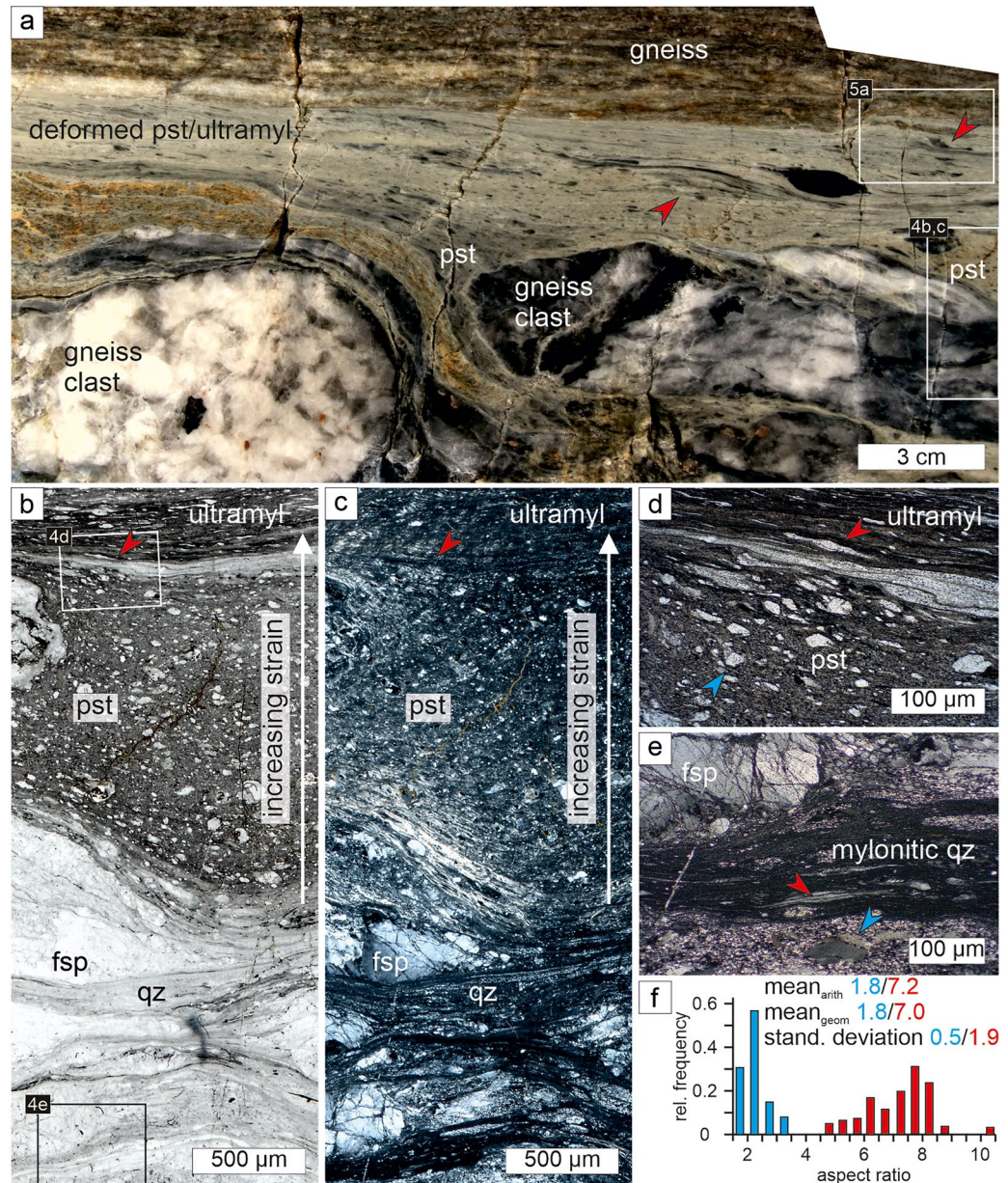
Figure 4. Deformed pseudotachylyte (pst) containing large gneiss clasts of feldspar (fsp) and quartz (qz) grading into an ultramylonitic layer (ultramyl), sample LB28. (a) Field and (b, c) thin section micrographs, respectively, (c) is taken with crossed polarizers. Aspect ratio of clasts is increasing and the spacing of the foliation is decreasing from the preserved pseudotachylyte at the bottom, finally grading to an ultramylonite at the top. Note mylonitic quartz clasts (red arrows). (d, e) Polarized light micrographs (crossed polarizers) of the gradual transition from pseudotachylyte to ultramylonite. Note mylonitic quartz clasts with a high aspect ratio in the ultramylonite (red arrows) and isometric quartz clasts in the preserved pseudotachylyte (blue arrows). (f) Aspect ratio of parent quartz clasts (blue) and mylonitic quartz clasts (red) within deformed pseudotachylyte and ultramylonite, respectively.

(SPO) (Figures 4a–4e). The aspect ratio of clasts gradually increases with a decreasing spacing of the foliation grading toward ultramylonite layers. In the strain shadow of the rigid gneiss clasts, the original fabric of the pseudotachylyte can be preserved with rounded and isometric clasts (Figures 4a–4c).

Characteristic ultramylonitic parts are defined by a fine-grained (<10 µm) mica-rich matrix with elongated larger mylonitic quartz clasts (Figures 4b–4e and 5a–5c). The mylonitic quartz clasts have a high aspect ratio of 7.0 ± 1.9 (long axis: 350–2,000 µm; short axis: 50–250 µm), which is considerably larger than that of the clasts within the
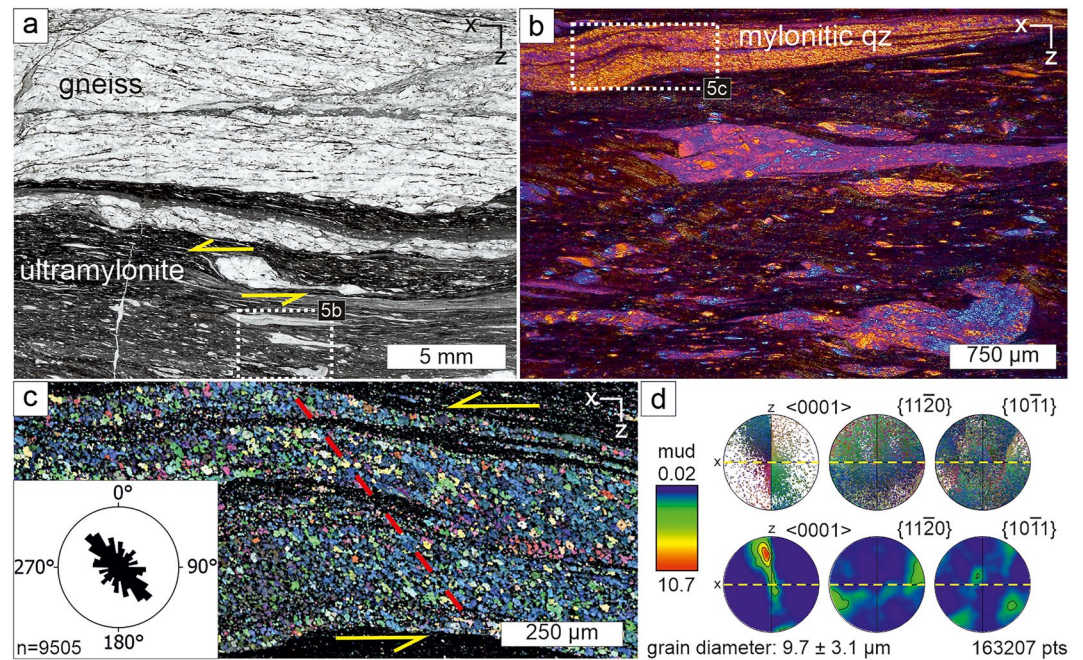
Figure 5. Mylonitic quartz microfabric in clasts of ultramylonite, sample LB28a. (a) Thin section micrograph of ultramylonite layer in contact with the host gneiss (position is shown in Figure 4a). A sinistral shear sense (yellow arrows) is indicated by asymmetric strain shadows around feldspar clasts within the fine-grained ultramylonite. (b) Polarized light micrograph (crossed polarizers and compensator plate inserted) of the ultramylonite containing mylonitic quartz (qz) clasts. (c) Electron backscattered diffraction map displaying different crystallographic orientations (all Euler angles) of mylonitic quartz. Recrystallized small grains show an oblique shape-preferred orientation (SPO) with the long axis at 30°–45° to the ultramylonite foliation, indicating a sinistral sense of shear (yellow arrows). The SPO is visualized by the inserted rose diagram and indicated with a red dashed line. (d) Stereographic projections (colors correspond to all Euler angle colors in (c)) and density plots of recrystallized quartz. The foliation of the ultramylonite is indicated by a yellow dashed line.

preserved pseudotachylyte of 1.8 ± 0.5 (long axis: 150–600 μm; short axis: 50–350 μm; Figures 4d–4f). Larger feldspar (albite) clasts are cataclastically deformed (Figures 4b, 4c, and 4e). The recrystallized quartz grains show an oblique SPO with the long axes of grains at an angle of about 30–45° to the ultramylonitic foliation (Figure 5c). They reveal a marked CPO characterized by a girdle maximum at a high angle to the stretching lineation of the gneiss (X, Figures 5c and 5d). The ⟨a⟩-axes are preferentially oriented in a plane about 10–20° to the foliation (Figure 5d). This quartz fabric with CPO and oblique SPO (Figures 5c and 5d) indicates dynamic recrystallization (strain-induced grain boundary migration) during shearing. The sinistral shear sense is consistent with asymmetric strain shadows around feldspar clasts within the ultramylonite (Figure 5a), indicating that the deformation of clasts is related to the formation of the ultramylonite and does not represent an inherited fabric.

4.3. Folded Injection Veins Crosscut by Pristine Pseudotachylytes

Folded and foliated injection veins (pst1) occur in deformed vein-quartz and are crosscut by pristine pseudotachylytes (pst2 and 3; Figures 2f and 6 and Figure S2 in Supporting Information S1). We first describe the pseudotachylytes and then the quartz microfabrics of the hosting quartz vein.

4.3.1. Pseudotachylytes

The folded and foliated injection veins (pst1; Figures 6a and 6b and Figure S2 in Supporting Information S1) display a fine-grained foliated matrix of quartz, feldspar, mica, and epidote, that also contains quartz-rich clasts with diameters <50 μm (Figures 6a and 6b and Figures S2c and S2d in Supporting Information S1). The foliation is defined by the SPO of the matrix minerals, including the epidote-feldspar aggregates, and corresponds to the foliation of the hosting deformed quartz vein (Figures 6b–6e and Figures S2c and S2d in Supporting Information S1).

The pristine pseudotachylyte (pst2) contains isometric quartz-rich clasts (<500 μm) (Figures 6a, 6b, and 6f) and larger clasts of amphibole-rich and biotite-rich gneisses (<3 cm) (Figures 6a and 6b). Hornblende shows $(\bar{1}01)[101]$
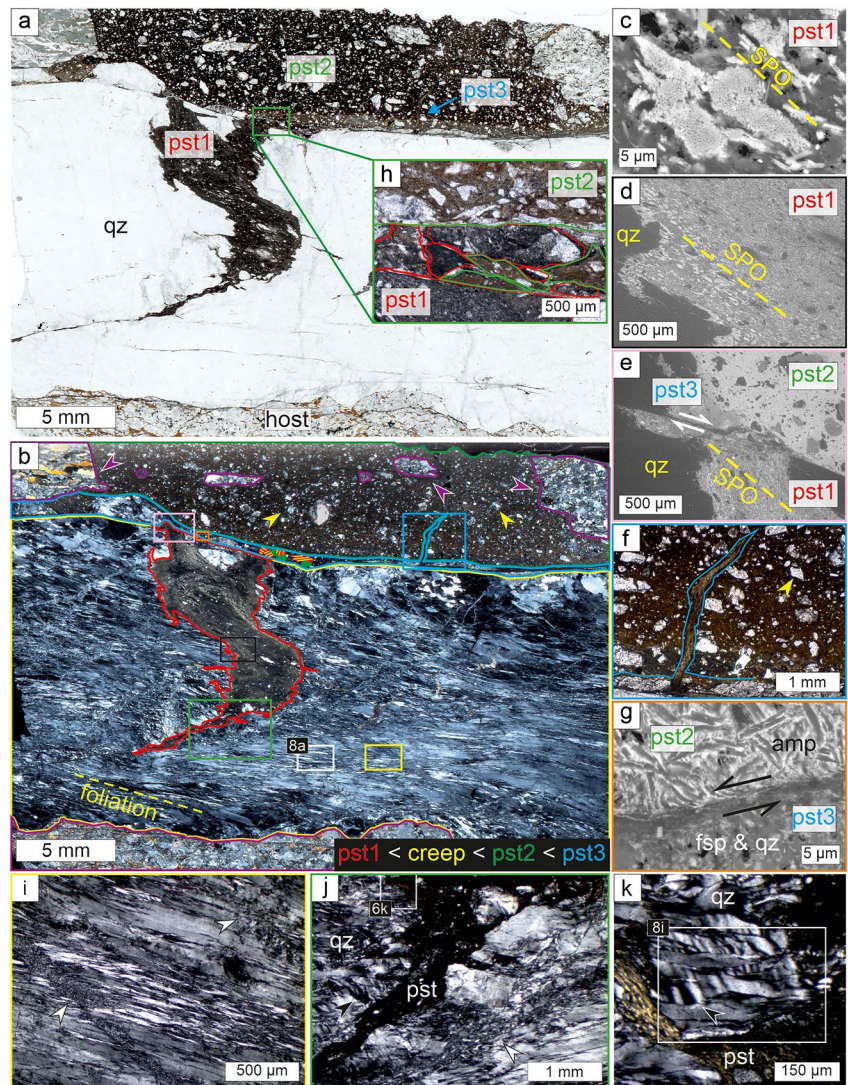
Figure 6. Microfabrics of deformed pseudotachylyte injection vein within deformed quartz vein, crosscut by pristine pseudotachylytes, sample LB78b. (a, b) Thin section scans (position is shown in Figure 2f) showing deformed pseudotachylyte injection vein (pst1, red) in a quartz-rich (qz) layer concordant to a biotite-rich host gneiss (bottom). Younger pristine pseudotachylyte (pst2, green) with clasts of amphibole-rich gneiss (purple arrows) and undeformed quartz (yellow arrows) crosscuts the folded injection vein. At the contact between the deformed (pst1, red) and pristine (pst2, green) pseudotachylyte, a third pseudotachylytic vein (pst3, blue) is present. Colored rectangles give the position of (d–j), respectively. (c–e) Backscattered electron (BSE) images of the different pseudotachylyte generations. (c) Matrix of deformed pseudotachylyte (pst1, position shown in Figure S2d in Supporting Information S1), which is composed of intergrown aggregates of epidote and plagioclase. The aggregates display an shape-preferred orientation (SPO) (yellow dashed line) that relates to the SPO of the hosting quartz layer. (d) Intergrown epidote-feldspar aggregates with SPO (yellow dashed line). (e) Deformed pseudotachylyte (pst1) with an SPO (yellow dashed line) and pristine pseudotachylyte (pst2) separated by a thin pseudotachylyte layer (pst3) indicating a dextral shear offset of pst1 (white arrows). (f) Polarized light micrograph of an injection vein of the third pseudotachylyte (pst3, blue) penetrating the pristine pseudotachylyte (pst2), which contains undeformed rounded quartz clasts (yellow arrow). (g) BSE image of pristine pseudotachylyte (pst2, green) containing sheared skeleton-shaped amphibole (amp) microliths indicating a sinistral sense of shearing (black arrows) at the sharp contact with the third pseudotachylyte (pst3, blue), which is mainly composed of feldspar (fsp) and quartz. (h) Polarized light micrograph of the contact between the deformed (pst1, red) and pristine (pst2, green) pseudotachylyte with rotated clasts of both pseudotachylytes. (i–k) Polarized light micrograph (crossed polarizers) showing quartz vein microfabric. (i, j) Foliated quartz is crosscut by networks of small new grains (white arrows). (k) Quartz associated with pseudotachylyte displaying short wavelength undulatory extinction (SWUE, black arrow).

mechanical twins, as generally found in pseudotachylyte-bearing amphibole-rich gneisses of the Silvretta (Brückner & Trepmann, 2021). The matrix of these pristine pseudotachylytes comprises homogenous skeleton-shaped amphibole microliths with a grain size of ~5 μm (pst2, Figure 6g), in detail described by Koch and Masch (1992).

The deformed pseudotachylyte (pst1, red in Figures 6a and 6b) and the pristine pseudotachylyte (pst2, green in Figures 6a and 6b) are separated by another thin (<100 μm in width) pseudotachylyte layer (pst3, blue in Figures 6a, 6b, and 6e–6g). Locally a shear offset to the deformed pseudotachylyte (pst1) of a few hundred μm can be observed (Figure 6e). The third pseudotachylyte (pst3, blue) also forms an injection vein within the pristine pseudotachylyte (pst2) (Figures 6a, 6b, and 6f). It is mainly composed of feldspar, quartz, and amphibole (Figure 6g) and shows a sharp boundary between the deformed (pst1, red) and pristine (pst2, green) pseudotachylyte (Figures 6e–6g). Rotated and brecciated clasts of both pseudotachylytes (pst1 and pst2) are embedded within that thin pseudotachylyte layer (pst3) (Figures 6a, 6b, and 6h). At the contact with the third pseudotachylyte, the amphibole microliths of the pristine pseudotachylyte matrix (pst2, green) are sheared (Figure 6g).

4.3.2. Microfabric of Hosting Quartz Vein

The hosting quartz vein shows a foliation that corresponds to that of the folded and foliated pseudotachylyte injection vein (Figures 6b–6e and 6i and Figures S2b–S2d in Supporting Information S1). The coarse elongate grains have long axes of several hundreds of μm to mm and aspect ratios of 5.0 ± 1.8 (Figures 6i, 6j, 7, and 8). They contain low-angle grain boundaries that define subgrains of similar shape and aspect ratio (Figures 7a and 7b). The CPO is characterized by a marked point maximum of ⟨c⟩-axes at a high angle to both the stretching lineation (X) and the normal to the foliation (Z) of the host gneisses, close to the Y-axis (Figures 7c and 8d). Small isometric grains (6 ± 3 μm in diameter) can be found mantling the coarse elongate grains (Figures 7a and 7b). Their orientations show a weaker maximum around Y, almost forming a girdle-maximum in the YZ-plane (Figure 7d), indicating a crystallographic control originating from the mantling coarse high aspect-ratio grains but also new orientations with ⟨c⟩-axes closer to Z.

In the vicinity of pseudotachylyte veins and their tips, fine quartz grains, <5 μm in diameter, occur (Figures 7a, 7b, and 8a–8c; yellow area). The CPO of these tiny quartz grains surrounding the pseudotachylyte is weak to almost absent with a preferred orientation of ⟨c⟩-axes closer toward a horizontal orientation at a small angle to Z (Figures 7e, 7f, and 8e). The misorientation angle distribution of the grains reveals an almost random crystallographic orientation (Figures 7h and 8g). In contrast, the small grains surrounding the larger grains show a higher abundance of low misorientation angles with a deficit of high misorientation angles compared to a random orientation (Figure 7g).

The foliation can be crosscut by fine-grained quartz aggregates that form irregular networks (Figures 6b, 6i, 6j, and 8a–8c, white area, and Figures S2b and S2c in Supporting Information S1), as well as fractures offsetting the elongate grains (Figures 8a–8c). The fine-grained aggregates contain isometric grains, of about 3.1 ± 1.5 μm in diameter showing a large orientation scatter and an almost random orientation similar to those in the vicinity of the pseudotachylytes (Figures 8e–8h). The grains in the networks exhibit low internal misorientations with angles below a few degrees (Figures 8c and 8h). Locally, along these fine-grained networks, an offset of the elongated large quartz grains can be observed (Figures 8a and 8b, white conjugated arrows). Associated with these networks of fine-grained quartz aggregates and pseudotachylyte injection veins, the coarse elongate quartz grains can show domains with a width of 10–50 μm and a spacing of 30–80 μm, characterized by alternating domains with different crystallographic orientations (Figures 6k and 8i). The relative misorientation angles are between 15° and 30° and the domain boundaries are oriented parallel to the short axis of the elongate quartz grains and subparallel to a {11$\bar{2}$0} prism plane (Figures 6k, 8i, and 8j). This alternating change in the crystallographic orientation, especially visible in the relative misorientation map (Figure 8i), is contrasting with a systematically increasing orientation change over otherwise similar deformation bands. Thus, these microstructures may rather be compared to kink bands, where, however, the kink band boundaries typically have a more abrupt change in crystallographic orientation. Due to the alternating change in orientation over the boundaries subparallel to a {11$\bar{2}$0} prism plane (Figure 8i), these domains are referred to as short wavelength undulatory extinction (SWUE, Trepmann & Stöckhert, 2013).

4.4. Brecciated Foliated Pseudotachylytes

Foliated pseudotachylyte clasts can occur embedded in a pristine pseudotachylyte vein (a few tens of mm to cm in width) concordant to the foliation of the host gneiss (Figures 9a and 9b). These foliated pseudotachylyte clasts are

several hundreds of μm in size (Figures 9b and 9c) and are comprised of fine-grained layers of quartz, albite, and amphibole. Quartz and albite clasts within the main pseudotachylyte vein can be somewhat larger with diameters of several hundreds of μm. The microstructure of the brecciated pseudotachylyte is fine-grained and the mineral content is similar to other deformed pseudotachylytes. Quartz layers (few tens of μm; aspect ratio 3.7 ± 1.1) in clasts show a very weak CPO (Figure 9d). The grain diameter of the quartz grains in the matrix within the clasts of 2.8 ± 1.0 μm is similar to that in the layers of 3.9 ± 2.0 μm, combined with an almost absent CPO (Figure 9e).

5. Discussion

Clasts of foliated pseudotachylytes in a pseudotachylyte breccia indicate two independent stages of coseismic rupturing separated by a stage of creep (Figures 2a, 2b, 2e, 6h, and 9). Likewise, the deformed pseudotachylytes forming ultramylonites and the folded injection veins (pst1), cut off by pristine pseudotachylytes (pst2), unambiguously indicate two independent stages of seismic rupturing separated by a stage of aseismic creep with dynamic recrystallization of quartz (Figures 2f–2h and 4–6). In contrast, pseudotachylytes (pst3) offsetting and crosscutting pristine (pst2) pseudotachylytes (Figure 6 and Figures S2a and S2b in Supporting Information S1), may reflect brittle deformation of an earlier and quenched pseudotachylyte with a somewhat later pseudotachylyte during complex rupturing, as opposed to representing another independent stage of rupturing. We discuss first the recorded deformation conditions during pseudotachylyte formation and creep, second the implications for the strength of the various fault rocks during the different stages, and third the assignment of the recorded coseismic rupturing events to the Alpine stages.

5.1. Deformation Conditions

Pseudotachylytes are especially common at the base of the seismogenic zone of the continental crust (i.e., temperatures of 300–350°C; 10–15 km depth), which corresponds to lower greenschist facies conditions (e.g., Allen, 2005; Hobbs et al., 1986; Lin et al., 2005; Price et al., 2012; Scholz, 2002; Shaw & Allen, 2007; Sibson, 1975, 1977, 1980; White, 1996). At these depths, modification of the microfabrics formed during high-stress crystal plasticity and fault healing during interseismic creep play an important role (e.g., Nüchter & Stöckhert, 2007; Trepmann et al., 2017; Trepmann & Stöckhert, 2003; Williams & Fagereng, 2022). The well-documented spatial relation of the fault rocks to the base of the Silvretta nappe relates their formation to the Alpine orogeny (Koch, 1990; Koch & Masch, 1992; Laubscher, 1983; Schmutz, 1995), during which the rocks experienced maximum pressure-temperature conditions of 350–540°C and 300–400 MPa (Hurford et al., 1989; Maggetti & Flisch, 1993; Thöni, 1981).

Similar to our findings, Pittarello et al. (2022) described two different generations of Silvretta pseudotachylytes (deformed and pristine pseudotachylytes). These authors, however, suggested their formation at different ambient pressure-temperature conditions. Older deformed pseudotachylytes with epidote aggregates were assumed to have formed at greenschist facies conditions and the pristine pseudotachylytes with skeletal intergrowth of plagioclase-amphibole aggregates at temperatures <250°C, respectively. Yet, our study confirms, that the phase assembly in the described pseudotachylytes (deformed and pristine) is mostly controlled by the host lithology, which has already been reported by Koch and Masch (1992). The occurrence of the epidote-feldspar intergrowth in pseudotachylytes (Figures 3 and 6c) can be associated with biotite-rich host gneisses, whereas the skeletal intergrowth of plagioclase-amphibole in pseudotachylytes (Figure 6g) is associated with amphibole gneisses. Likewise, stilpnomelane is occurring in pristine (Figures 3a and 3c) and deformed pseudotachylytes (Figures 3d and 3f). These observations suggest that the deformed, as well as the pristine pseudotachylytes experienced greenschist facies conditions during or after their formation.

The stage of creep is characterized by dislocation creep of quartz with ⟨a⟩-dislocation glide and associated recovery and recrystallization (i.e., dynamic strain-induced grain boundary migration). This is recorded by the CPO and oblique SPO of recrystallized quartz within the ultramylonites (i.e., deformed pseudotachylytes) (Figures 5c and 5d), as well as the CPO and SPO in the host quartz layer associated with the SPO of folded injection veins (Figures 7 and 8). This relative homogeneous recrystallization-microfabric with oblique SPO and well-developed CPO (Figures 5c and 5d), is indicating efficient dislocation climb, which is thermally activated and requires diffusion, and thus at least lower greenschist facies conditions (e.g., Stipp et al., 2002; Stöckhert et al., 1999). Therefore, ultramylonites and mylonites (Figures 2g, 2h, 4, and 5) record a stage of creep at temperatures of at
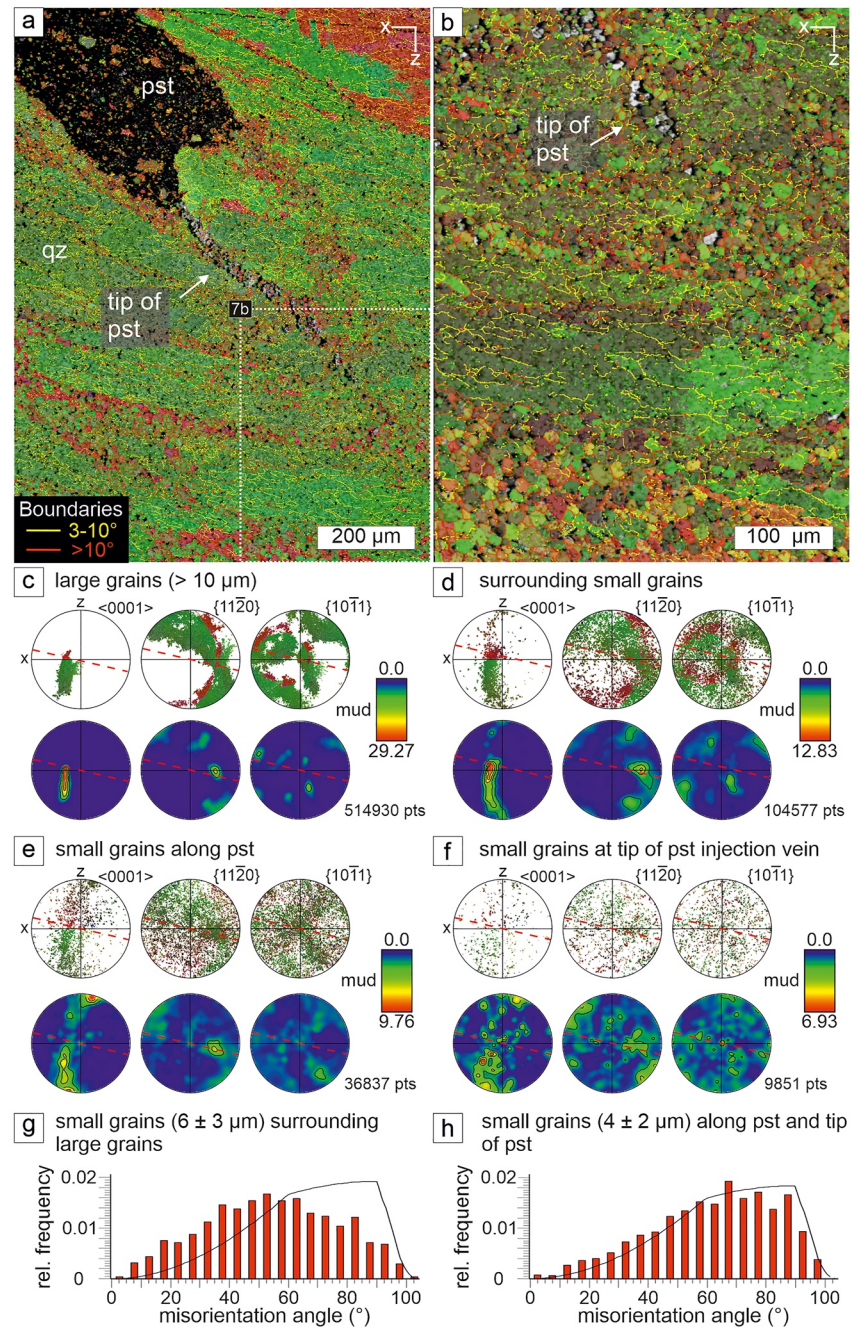
Figure 7. Electron backscattered diffraction data of quartz (qz) hosting deformed pseudotachylyte (pst) injection veins, sample LB78d (position is shown in Figure S2b in Supporting Information S1). (a, b) Map displaying different quartz crystallographic orientations (all Euler angle), as well as high- (red) and low-angle (yellow) grain boundaries. Vein quartz shows large grains with shape-preferred orientation surrounded by smaller grains. (c–f) Stereographic projections (colors correspond to all Euler angle colors in (a) and (b)) and density plots of coarse high-aspect ratio grains, small grains surrounding the latter, as well as small grains surrounding and at the tip of pseudotachylytes, respectively. The foliation is indicated by the red dashed line. (g, h) Misorientation angle distribution of small quartz grains surrounding large grains and along the pseudotachylyte injection vein and its tip, respectively. Theoretic random distribution is shown by the black solid line.

least greenschist facies conditions before the formation of the crosscutting pristine pseudotachylytes (Figure 6, pst2 and pst3). Overall, the greenschist facies conditions documented by (a) stilpnomelane and epidote present in deformed and pristine pseudotachylytes and (b) dislocation creep of quartz in deformed pseudotachylytes
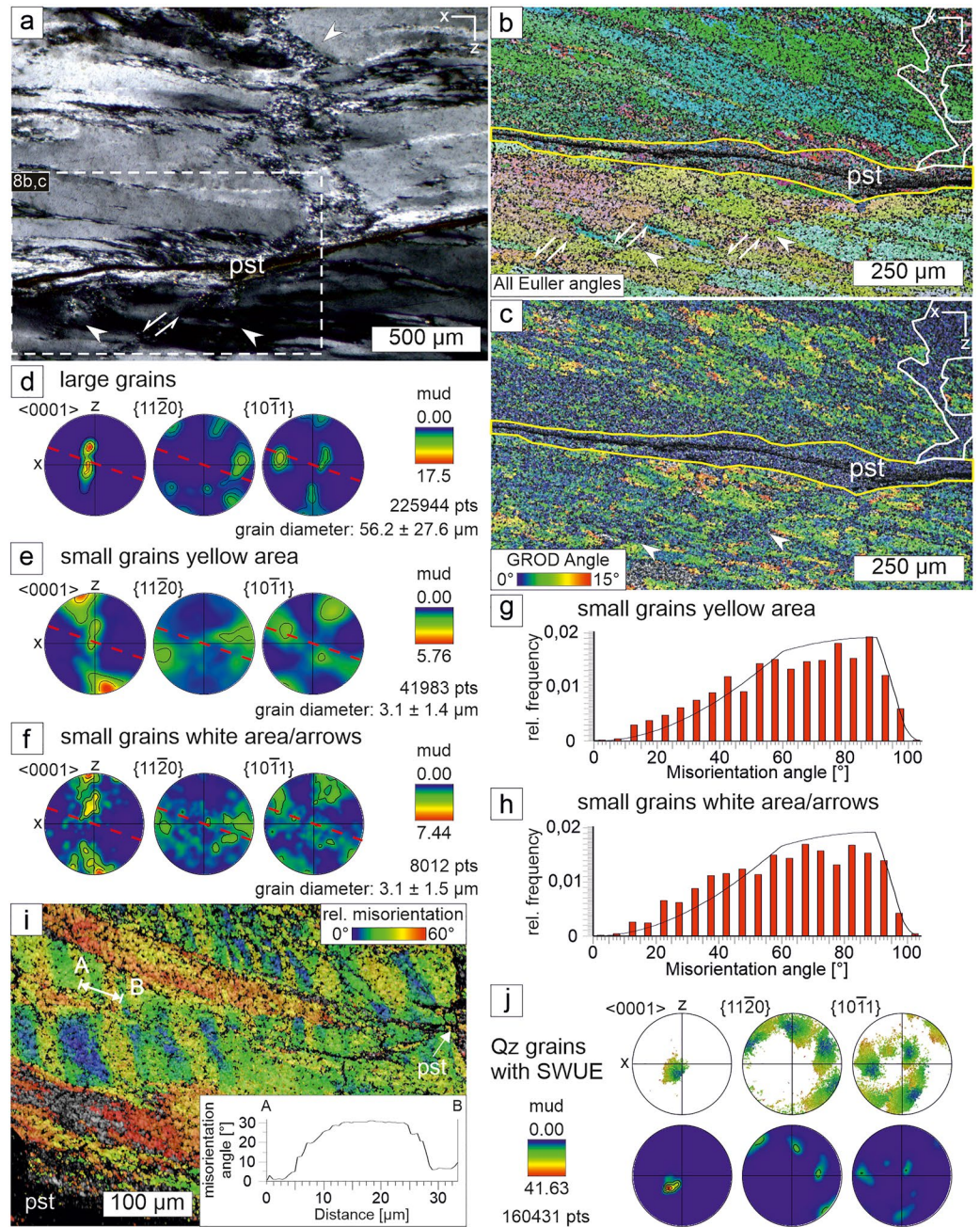
Figure 8. Quartz microfabrics in the vicinity of pseudotachylytes, sample LB78b. (a) Polarized light micrograph (crossed polarizers, position is shown in Figure 6b) of quartz vein containing pseudotachylytes (pst), that displays large grains with shape-preferred orientation surrounded by smaller grains. Irregular networks of fine-grained isometric quartz aggregates in special relation to pseudotachylytes are shown by white arrows. (b, c) Electron backscattered diffraction (EBSD) maps display different crystallographic orientations (all Euler angles) and Grain Reference Orientation Distribution (GROD; deviation angle from mean grain orientation plotted for each pixel), respectively. (d–f) Density plots (stereographic projections) for indicated quartz aggregates. The foliation is demonstrated with a red dashed line. (g, h) Misorientation angle distribution of small quartz grains along the pseudotachylyte injection vein and in discordant networks (yellow area and white area/arrows in (b) and (c), respectively). Theoretic random distribution is shown by the black solid line. (i) EBSD map displaying relative misorientation angle distribution and profile along AB line over domains characterized by an alternating change in crystallographic orientation (short wavelength undulatory extinction [SWUE]) with boundaries subparallel to $\{11\bar{2}0\}$. (j) Stereographic projections (colors correspond to relative misorientation colors in (i)) and density plots of quartz grains with SWUE.
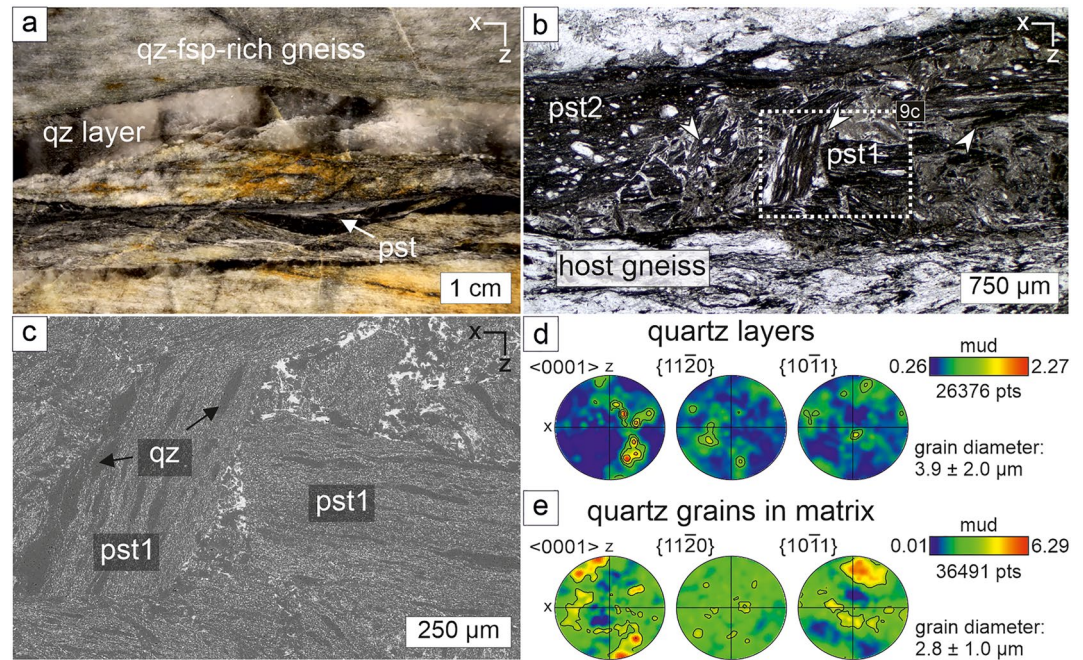
Figure 9. Foliated pseudotachylyte clasts in pseudotachylyte layer concordant to quartz veins in host gneiss, sample LB24. (a) Quartz-feldspar-rich host gneiss (qz; fsp) containing concordant pseudotachylyte (pst) and quartz layers. (b) Polarized light micrograph of a concordant and brecciated pseudotachylyte layer, containing rotated clasts of pseudotachylytes (white arrows), representing the first generation of pseudotachylyte (pst1) embedded in a second generation (pst2). (c) Backscattered electron (BSE) image of rotated foliated pseudotachylyte clasts comprised of fine-grained layers of quartz, albite, and amphibole. (d, e) Density plots (stereographic projections) of quartz in layers and quartz within the matrix of the first generation of pseudotachylyte.

precludes that the pristine pseudotachylytes formed at much lower ambient temperature conditions. Thus, we conclude that all recorded deformation stages occurred at similar ambient greenschist facies conditions.

It is known that different deformation mechanisms documented by pseudotachylytes, mylonites, and ultramylonites do not necessarily reflect differences in ambient temperature-pressure conditions but can likewise reflect changing stress- and strain rate conditions during the seismic cycle at an approximately constant crustal level (e.g., Matysiak & Trepmann, 2012; Nüchter et al., 2013; White, 2012). The Silvretta pseudotachylyte formation is related to transient coseismic high-strain/high-stress deformation at >400 MPa differential stress, recorded by $(\bar{1}01)$ mechanical amphibole twins (Brückner & Trepmann, 2021), and associated with quartz microfabrics indicating high-stress crystal plasticity (Trepmann et al., 2017). The stresses during creep estimated by the quartz recrystallization-microfabric with grain diameters on the order of 10 μm (Figure 5) were on the order of hundred MPa, applying the quartz recrystallization grain size paleopiezometer of Stipp and Tullis (2003). As there is no evidence of different pressure-temperature conditions, as discussed above, the recorded changes in deformation mechanisms and different stress and strain-rate conditions are explained by the dependence on the distance to the propagating fault tip during the decoupling of the Silvretta nappe from its original basement, following the model by Nüchter et al. (2013). These authors explained the systematic sequence of ductile and subsequently brittle deformation mechanisms at constant ambient pressure-temperature conditions by a decreasing distance to the propagating seismic active thrust tip. Accordingly, the Silvretta pseudotachylytes represent deformation during seismic rupturing, that is, high stress and/or strain-rate conditions, whereas (ultra-)mylonites indicate a stage of creep at a larger distance to the active rupture tip, that is, lower stress and strain-rate conditions.

5.2. Relative Strength of Pseudotachylytes and Host Rocks

The model of Nüchter et al. (2013) requires that during thrust growth coseismic strain is localized in the previously unaffected rock leading eventually to nappe decoupling from its basement. On the other hand, pseudotachylytes are commonly taken as a weak phase (Guermani & Pennacchioni, 1998; Passchier, 1982; Passchier &

Trouw, 2005; Passelègue et al., 2021; Price et al., 2012), allowing strain localization at low shear stresses during subsequent nappe transport, especially in the presence of fluid phases allowing for dissolution precipitation creep (Bachmann et al., 2009; Cook & Aitken, 1976; Davis & Engelder, 1985; Davis et al., 1983; King Hubbert & Rubey, 1959; Koch & Masch, 1992; Laubscher, 1983; Rodgers et al., 1962). Taking these two findings together suggests that pseudotachylytes have a higher strength during coseismic high-stress crystal plasticity than the host rock but a lower strength during creep. Whether the here described deformed and pristine pseudotachylytes can validate this hypothesis will be addressed in the following.

The fine-lamellar foliated ultramylonitic matrix (i.e., deformed pseudotachylyte), deflected by the ellipsoid clasts of host gneiss (Figures 2g, 2h, 4, 5a, and 5b), gives evidence that the fine-grained and polyphase pseudotachylytes are accumulating a higher amount of strain during creep compared to the host gneiss. This observation confirms that during creep, the pseudotachylytes represent the lithology of lower strength compared to the host gneisses, including the coarse-grained quartz vein, consistent with what is reported from other studies (Bachmann et al., 2009; Cook & Aitken, 1976; Davis & Engelder, 1985; Davis et al., 1983; King Hubbert & Rubey, 1959; Koch & Masch, 1992; Laubscher, 1983; Rodgers et al., 1962).

The networks of small isometric new quartz grains (<5 μm) either aligned along the second pristine pseudotachylytes (Figures 8a–8c) or discordant to the SPO of the foliated host quartz vein, indicate nucleation and growth along former highly damaged zones, that are related to the second coseismic deformation event (e.g., Trepmann et al., 2007). These new grains in the networks are strain-free, revealing that they grew at quasi-isostatic stress conditions, that is, they record fast stress relaxation after transient peak stresses (Trepmann et al., 2017). Furthermore, high aspect-ratio quartz grains in the host veins related to networks of new grains and pseudotachylytic veins display SWUE (Figures 6k, 8i, and 8j). These microfabrics overprinting the foliated quartz veins indicate high-stress dislocation glide-controlled deformation associated with microfracturing (e.g., Trepmann et al., 2017; Trepmann & Stöckhert, 2013) during the last stage of pseudotachylyte formation and after the stage of creep. In contrast, evidence of comparable high-stress crystal plasticity in the first generation of pseudotachylyte (pst1) is not apparent. Thus, during coseismic high-stress deformation, the coarse-grained quartz is accumulating a higher amount of strain than the associated pseudotachylytes and develops microstructures indicative of high-stress crystal plasticity, that is, they have a lower strength. This is consistent with the Hall-Petch relation that smaller grain sizes impede dislocation glide (Fredrich et al., 1990; Hall, 1951; Hirth, 1972; Petch, 1953). Furthermore, "*kick-cook-kick*" experiments (Trepmann et al., 2013), simulating a cycle of coseismic loading, postseismic relaxation, and a second coseismic loading event suggest, that strain during the second transient high-stress deformation event is not localized in the same rock volume again.

Consistently, also mylonites and ultramylonites are less commonly found to contain pseudotachylytes (Koch & Masch, 1992; Schmutz, 1995). The indication of higher strength during high-stress plasticity of coarse gneisses in comparison to finer grained mylonites, ultramylonites, and pseudotachylytes can explain, that during the successive seismic event only those rocks, which have not been previously affected, rupture. This finding would be consistent with the concept that seismic rupturing is more likely in rock volumes with higher stored elastic strain energy (Cocco et al., 2023; Scholz, 2002), which might be the case for rocks that have not previously experienced aseismic creep, compared to those that have experienced previous creep.

Overall, our observations indicate that pseudotachylytes accumulate a higher amount of strain during creep at a larger distance to the fault tip compared to the gneisses. In contrast, the coarse gneisses accumulate a higher amount of strain during coseismic high-stress crystal plasticity. Such "inverse" strength relationship during deformation at different distances to the tip of the seismic active fault (i.e., at different stress and strain-rate conditions and similar pressure-temperature conditions) has been similarly found in the Silvretta fault rocks for amphibole-rich gneisses and quartz veins. There, amphibole represents the lower strength phase during transient high-stress coseismic deformation, but the higher strength phase during creep, given the lower fracture toughness, the higher shear modulus, and the lower melting temperature of amphibole relative to quartz (Brückner & Trepmann, 2021).

5.3. Relation to Alpine Stages

Our observations are in accord with earlier interpretations that the Silvretta pseudotachylytes represent seismic rupturing during the decoupling of the crystalline nappe from its original basement, given the widespread
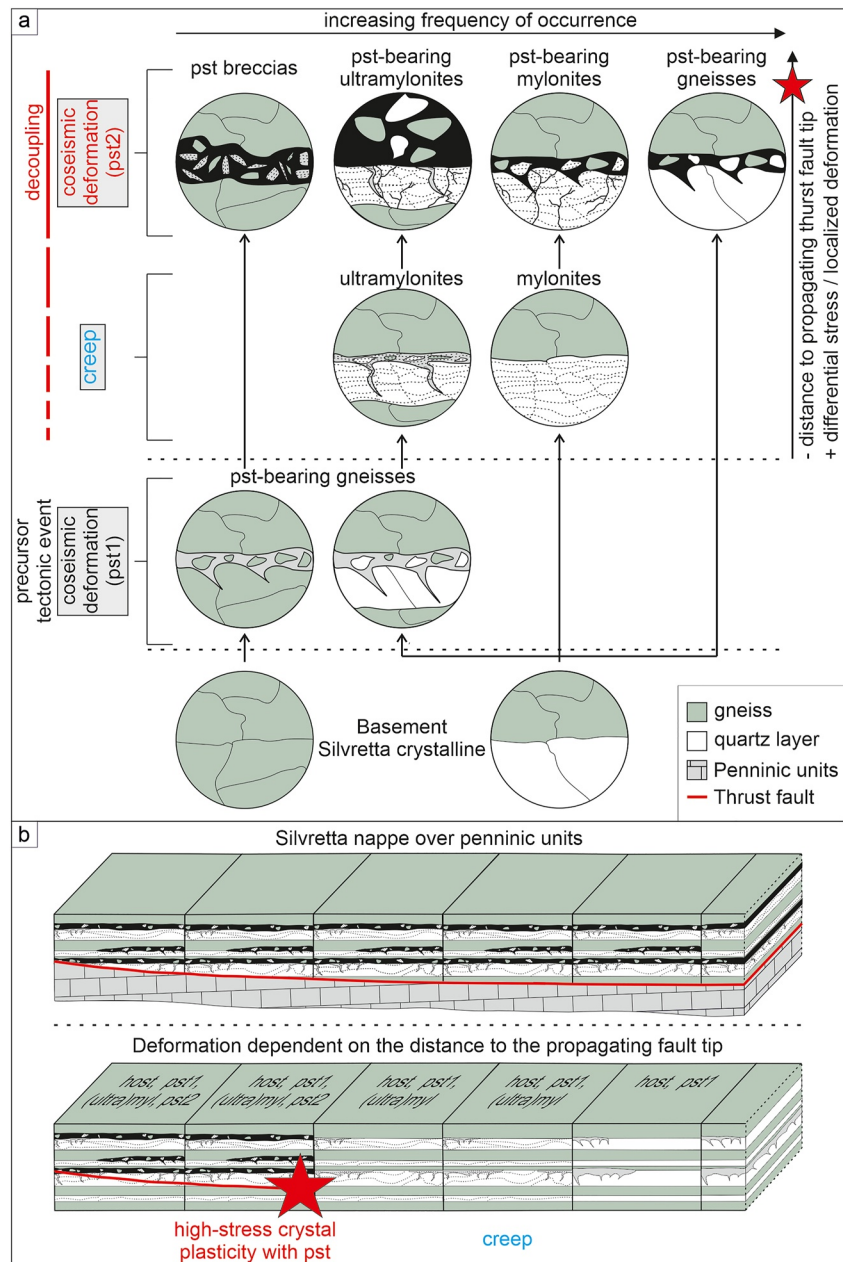
Figure 10. Conceptual sketch showing (a) the formation of the various Silvretta fault rocks in dependence on the distance to the propagating thrust tip during the decoupling of the nappe (b) following the model after Nüchter et al. (2013). See text for discussion.

occurrence of fault rocks restricted to 300 m of the base of the Silvretta nappe and no evidence of components of the footwall in pseudotachylytes (Insubric crystalline) (Koch & Masch, 1992; Laubscher, 1983; Schmutz, 1995; Thöni, 1988). Yet, we do not follow the interpretation of Koch and Masch (1992) that the decoupling occurred with a cyclic formation of pseudotachylytes and mylonites and that ultramylonites represent the latest stage formed at peak Eo-Alpine metamorphic conditions during transport of the nappe over the Penninic Units, as ultramylonites (deformed pseudotachylytes) and mylonites can be crosscut by pristine pseudotachylytes (Figures 6 and 10a). In contrast, both, mylonites and ultramylonites (i.e., the deformed first generation of pseudotachylytes) are interpreted to represent deformation at a large distance to the propagating thrust tip before the final decoupling, displayed by pristine pseudotachylytes (Figure 10a), following the model of Nüchter et al. (2013) (Figure 10b). The pristine pseudotachylytes represent the last microstructural imprint after the passage of the seismically active

fault tip of the affected rocks during the decoupling of the nappe from its original basement. The by far less common deformed pseudotachylytes are interpreted as an independent precursor tectonic event before the final decoupling (Figure 10a). This view does not exclude later localized deformation at the base of the nappe during transport dominated by dissolution precipitation creep at low stresses.

The peak metamorphic conditions in the Silvretta are dated to about 110–85 Ma (Hurford et al., 1989; Maggetti & Flisch, 1993; Thöni, 1981). Isotopic investigations of the pseudotachylytes indicate their formation in Late Cretaceous to Paleocene epochs ($^{87}Rb/^{86}Sr$ whole rock about 75 Ma: Thöni, 1988; $^{40}Ar/^{39}Ar$ whole rock 62–78 Ma: Bachmann et al., 2009), which is therefore likely the age of the final decoupling of the Silvretta nappe and in accord with our findings of deformation at greenschist facies conditions for the two stages of pseudotachylyte formation separated by a stage of creep (Figure 10a). However, the age determination of pseudotachylytes is hampered by the presence of abundant host rock clasts in the matrix (Bachmann et al., 2009; Thöni, 1988). Specific new radiometric dating of the various fault rocks and especially of the deformed pseudotachylytes would be required for a further assignment to the Alpine tectonic stages.

6. Conclusions

The described microstructures of the fault rocks from the base of the Silvretta nappe exemplify two stages of pseudotachylyte formation, reflecting coseismic transient high-stress (>400 MPa) deformation, which are separated by an intermediate stage of creep at lower stresses (on the order of hundred MPa) at similar greenschist facies conditions (Figure 10). The stage of creep is interpreted to represent deformation at larger distances to the propagating active thrust fault before the final stage of pseudotachylyte formation resulting in the decoupling of the nappe, which allowed the superposition onto the Penninic units. The deformed pseudotachylytes are taken to represent an independent earlier precursor tectonic event.

During creep, the fine-grained polyphase pseudotachylytes accumulate a higher amount of strain relative to the coarse host gneisses (Figures 4 and 5). In contrast, during coseismic high-stress crystal plasticity (associated microfracturing and dislocation glide), the coarser grained quartz-rich lithologies are accumulating a relatively higher amount of strain (Figure 7). During later modification at greenschist facies conditions and rapidly relaxing stresses, SWUE and networks of new grains along the damage zone of former microcracks within the mylonitic quartz vein formed (Figures 6–8).

The described microfabrics suggest that the specific stress and strain-rate conditions, dependent on the distance to the propagating seismic active fault tip, are decisive regarding the rheological behavior of crustal rocks at the base of the seismogenic zone during thrusting and do not reflect a change in pressure-temperature conditions. That the next rupturing event affects only rocks that have not been previously ruptured in the same event on one hand and that strain is localized in the fault rocks during creep on the other, demonstrates the importance of varying crustal rock strengths depending on specific stress and strain-rate conditions during the seismic cycle. Thus, modeling the strength of crustal blocks during orogeny requires distinguishing the rheology of rocks dependent on the distance to the seismic active fault tip.

Data Availability Statement

All data used for microstructural analyses in the study are available at Mendeley data (https://data.mendeley.com/) via https://data.mendeley.com/datasets/xhh2ktks9g/4 (DOI: 10.17632/xhh2ktks9g.4) with CC BY 4.0. Version 4.2 of the Aztec software (Oxford Instruments, 2020), used for microstructural data acquisitions, is available at https://nano.oxinst.com/products/aztec/. Version 6.6.1 of the LabSpec software (Horiba Scientific, 2022), used for Raman processing and analysis, is available at https://www.horiba.com/aut/scientific/products/detail/action/show/Product/labspec-6-spectroscopy-suite-software-1843/. Figures were made with CorelDRAW 2021 (64 bit) version 23.1.0.389 (Corel Corporation, 2022), available under the CorelDRAW license at https://www.coreldraw.com.

References

Allen, J. L. (2005). A multi-kilometer pseudotachylyte system as an exhumed record of earthquake rupture geometry at hypocentral depths (Colorado, USA). *Tectonophysics*, *402*(1–4 SPEC. ISS), 37–54. https://doi.org/10.1016/j.tecto.2004.10.017

Altenberger, U., Prosser, G., Grande, A., Günter, C., & Langone, A. (2013). A seismogenic zone in the deep crust indicated by pseudotachylytes and ultramylonites in granulite-facies rocks of Calabria (Southern Italy). *Contributions to Mineralogy and Petrology*, *166*(4), 975–994. https://doi.org/10.1007/s00410-013-0904-3

Altenberger, U., Prosser, G., Ruggiero, M., & Günter, C. (2011). Microstructure and petrology of a Calabrian garnet-bearing pseudotachylyte - A link to lower-crustal seismicity. *Geological Society Special Publication*, *359*(1), 153–168. https://doi.org/10.1144/SP359.9

Bachmann, R., Oncken, O., Glodny, J., Seifert, W., Georgieva, V., & Sudo, M. (2009). Exposed plate interface in the European Alps reveals fabric styles and gradients related to an ancient seismogenic coupling zone. *Journal of Geophysical Research*, *114*(5), 1–23. https://doi.org/10.1029/2008JB005927

Brückner, L. M., & Trepmann, C. A. (2021). Stresses during pseudotachylyte formation - Evidence from deformed amphibole and quartz in fault rocks from the Silvretta basal thrust (Austria). *Tectonophysics*, *817*(June), 229046. https://doi.org/10.1016/j.tecto.2021.229046

Campbell, L. R., & Menegon, L. (2019). Transient high strain rate during localized viscous creep in the dry lower continental crust (Lofoten, Norway). *Journal of Geophysical Research: Solid Earth*, *124*(10), 10240–10260. https://doi.org/10.1029/2019JB018052

Campbell, L. R., & Menegon, L. (2022). High stress deformation and short-term thermal pulse preserved in pyroxene microstructures from exhumed lower crustal seismogenic faults (Lofoten, Norway). *Journal of Geophysical Research: Solid Earth*, *127*(7), e2021JB023616. https://doi.org/10.1029/2021JB023616

Campbell, L. R., Menegon, L., Fagereng, Å., & Pennacchioni, G. (2020). Earthquake nucleation in the lower crust by local stress amplification. *Nature Communications*, *11*(1), 1–9. https://doi.org/10.1038/s41467-020-15150-x

Cocco, M., Aretusini, S., Cornelio, C., Nielsen, S. B., Spagnuolo, E., Tinti, E., & Di Toro, G. (2023). Fracture energy and breakdown work during earthquakes. *Annual Review of Earth and Planetary Sciences*, *51*(1), 217–252. https://doi.org/10.1146/annurev-earth-071822-100304

Cook, D. G., & Aitken, J. D. (1976). Two cross-sections across selected Franklin Mountain structures and their implications for hydrocarbon exploration. *Geological Survey of Canada*, *76*, 315–322.

Corel Corporation. (2022). Corel DRAW (Version 23.1.0.389) [Software]. Retrieved from https://www.coreldraw.com

Cowan, D. S. (1999). Do faults preserve a record of seismic slip? A field geologist's opinion. *Journal of Structural Geology*, *21*(8–9), 995–1001. https://doi.org/10.1016/S0191-8141(99)00046-2

Cowie, P. A., & Scholz, C. H. (1992). Displacement-length scaling relationship for faults: Data synthesis and discussion. *Journal of Structural Geology*, *14*(10), 1149–1156. https://doi.org/10.1016/0191-8141(92)90066-6

Davis, D. M., & Engelder, T. (1985). The role of salt in fold-and-thrust belts. *Tectonophysics*, *119*(1–4), 67–88. https://doi.org/10.1016/0040-1951(85)90033-2

Davis, D. M., Suppe, J., & Dahlen, F. A. (1983). Mechanics of fold-and-thrust belts and accretionary wedges. *Journal of Geophysical Research*, *88*(B2), 1153–1172. https://doi.org/10.1029/JB088iB02p01153

Dawers, N. H., Anders, M. H., & Scholz, C. H. (1993). Growth of normal faults: Displacement-length scaling. *Geology*, *21*(12), 1107. https://doi.org/10.1130/0091-7613(1993)021<1107:GONFDL>2.3.CO;2

Fredrich, J. T., Evans, B., & Wong, T.-F. (1990). Effect of grain size on brittle and semibrittle strength: Implications for micromechanical modelling of failure in compression. *Journal of Geophysical Research*, *95*(B7), 10907–10920. https://doi.org/10.1029/JB095iB07p10907

Froitzheim, N., Schmid, S. M., & Conti, P. (1994). Repeated change from crustal shortening to orogen-parallel extension in the Austroalpine units of Graubünden. *Eclogae Geologicae Helvetiae*, *87*(2), 559–612.

Grocott, J. (1981). Fracture geometry of pseudotachylyte generation zones: A study of shear fractures formed during seismic events. *Journal of Structural Geology*, *3*(2), 169–178. https://doi.org/10.1016/0191-8141(81)90012-2

Guermani, A., & Pennacchioni, G. (1998). Brittle precursors of plastic deformation in a granite: An example from the Mont Blanc massif (Helvetic, western Alps). *Journal of Structural Geology*, *20*(2–3), 135–148. https://doi.org/10.1016/S0191-8141(97)00080-1

Hall, E. O. (1951). The deformation and ageing of mild steel: III discussion of results. *Proceedings of the Physical Society. Section B*, *64*(9), 747–753. https://doi.org/10.1088/0370-1301/64/9/303

Hammer, W. (1914). Das Gebiet der Bündnerschiefer im tirolischen Oberinntal. *Jahrbuch der Kaiserlich Königlichen Geologischen Reichsanstalt*, *64*(3), 443–566.

Hawemann, F., Mancktelow, N. S., Wex, S., Camacho, A., & Pennacchioni, G. (2018). Pseudotachylyte as field evidence for lower-crustal earthquakes during the intracontinental Petermann Orogeny (Musgrave Block, Central Australia). *Solid Earth*, *9*(3), 629–648. https://doi.org/10.5194/se-9-629-2018

Heesakkers, V., Murphy, S., & Reches, Z. (2011). Earthquake rupture at focal depth, Part I: Structure and rupture of the Pretorius fault, TauTona mine, South Africa. *Pure and Applied Geophysics*, *168*(12), 2395–2425. https://doi.org/10.1007/s00024-011-0354-7

Hirth, J. P. (1972). The influence of grain boundaries on mechanical properties. *Metallurgical Transactions*, *3*(12), 3047–3067. https://doi.org/10.1007/BF02661312

Hobbs, B. E., Ord, A., & Teyssier, C. (1986). Earthquakes in the ductile regime? *Pure and Applied Geophysics PAGEOPH*, *124*(1–2), 309–336. https://doi.org/10.1007/BF00875730

Horiba Scientific. (2022). LabSpec 6 spectroscopy suite [Software]. Retrieved from https://www.horiba.com/aut/scientific/products/detail/action/show/Product/labspec-6-spectroscopy-suite-software-1843/

Hurford, A. J., Flisch, M., & Jäger, E. (1989). Unravelling the thermo-tectonic evolution of the Alps: A contribution from fission track analysis and mica dating. *Geological Society Special Publication*, *45*(1), 369–398. https://doi.org/10.1144/GSL.SP.1989.045.01.21

King Hubbert, M., & Rubey, W. W. (1959). Role of fluid pressure in mechanics of overthrust faulting: I. Mechanics of fluid-filled porous solids and its application to overthrust faulting. *Bulletin of the Geological Society of America*, *70*(2), 115–166. https://doi.org/10.1130/0016-7606(1959)70[115:ROFPIM]2.0.CO;2

Kirkpatrick, J. D., & Shipton, Z. K. (2009). Geologic evidence for multiple slip weakening mechanisms during seismic slip in crystalline rock. *Journal of Geophysical Research: Solid Earth*, *114*(12), B12401. https://doi.org/10.1029/2008JB006037

Koch, N. (1990). Licht- und elektronenmikroskopische Untersuchungen zur Deformationsgeschichte von Myloniten und Pseudotachyliten der Basis der Silvretta-Decke (Graubünden, Tirol) und Vergleich mit Myloniten der ZEV (Zone von Erbendorf-Vohenstraub, Oberpfalz) - Dissertati (Ph. D. thesis). Ludwig-Maximilians-University.

Koch, N., & Masch, L. (1992). Formation of Alpine mylonites and pseudotachylytes at the base of the Silvretta nappe, Eastern Alps. *Tectonophysics*, *204*(3–4), 289–306. https://doi.org/10.1016/0040-1951(92)90313-U

Laubscher, H. P. (1983). Detachment, shear, and compression in the central Alps. *Geological Society of America*, *158*, 191–211.

Lin, A. (2008a). *Fossil earthquakes: The formation and preservation of pseudotachylytes* (Vol. 111). Springer Berlin Heidelberg. https://doi.org/10.1007/978-3-540-74236-4

Lin, A. (2008b). Seismic slip in the lower crust inferred from granulite-related pseudotachylyte in the Woodroffe thrust, Central Australia. *Pure and Applied Geophysics*, *165*(2), 215–233. https://doi.org/10.1007/s00024-008-0301-4

Lin, A., Maruyama, T., Aaron, S., Michibayashi, K., Camacho, A., & Kano, K. (2005). Propagation of seismic slip from brittle to ductile crust: Evidence from pseudotachylyte of the Woodroffe thrust, central Australia. *Tectonophysics*, *402*(1–4), 21–35. https://doi.org/10.1016/j.tecto.2004.10.016

Lin, A., Sun, Z., & Yang, Z. (2003). Multiple generations of pseudotachylyte in the brittle to ductile regimes, Qinling-Dabie Shan ultrahigh-pressure metamorphic complex, central China. *Island Arc*, *12*(4), 423–435. https://doi.org/10.1046/j.1440-1738.2003.00407.x

Maggetti, M., & Flisch, M. (1993). Evolution of the Silvretta nappe. In J. F. Raumer & F. Neubaue (Eds.), *Pre-mesozoic geology in the Alps* (pp. 469–484). Springer Berlin Heidelberg.

Masch, L. (1970). *Die Pseudotachylite der Silvretta, eine Untersuchung ihrer Aufschmelzung und Deformation* (Dissertation). Ludwig-Maximilians-University.

Masch, L. (1974). Untersuchung der Aufschmelzung und Deformation der Pseudotachylite der Silvretta (Österreich, Schweiz). *Neues Jahrbuch Für Mineralgie - Monatshefte*, *11*, 485–509. https://doi.org/10.1127/njmm/1973/1974/485

Matysiak, A. K., & Trepmann, C. A. (2012). Crystal-plastic deformation and recrystallization of peridotite controlled by the seismic cycle. *Tectonophysics*, *530–531*, 111–127. https://doi.org/10.1016/j.tecto.2011.11.029

Menegon, L., Pennacchioni, G., Malaspina, N., Harris, K., & Wood, E. (2017). Earthquakes as precursors of ductile shear zones in the dry and strong lower crust. *Geochemistry, Geophysics, Geosystems*, *18*(12), 4356–4374. https://doi.org/10.1002/2017GC007189

Mitchell, T. M., Toy, V., Di Toro, G., Renner, J., & Sibson, R. H. (2016). Fault welding by pseudotachylyte formation. *Geology*, *44*(12), 1059–1062. https://doi.org/10.1130/G38373.1

Moecher, D. P., & Steltenpohl, M. G. (2009). Direct calculation of rupture depth for an exhumed paleoseismogenic fault from mylonitic pseudo-tachylyte. *Geology*, *37*(11), 999–1002. https://doi.org/10.1130/G30166A.1

Nüchter, J.-A., & Stöckhert, B. (2007). Vein quartz microfabrics indicating progressive evolution of fractures into cavities during postseismic creep in the middle crust. *Journal of Structural Geology*, *29*(9), 1445–1462. https://doi.org/10.1016/j.jsg.2007.07.011

Nüchter, J.-A., Wassmann, S., & Stöckhert, B. (2013). Cyclic ductile and brittle deformation related to coseismic thrust fault propagation: Structural record at the base of a basement nappe (Preveli, Crete). *Tectonics*, *32*(5), 1272–1293. https://doi.org/10.1002/tect.20079

Oxford Instruments. (2020). AZtec (Version 4.2) [Software]. Retrieved from https://nano.oxinst.com/products/aztec/

Passchier, C. W. (1982). Pseudotachylyte and the development of ultramylonite bands in the Saint-Barthdlerny Massif, French Pyrenees. *Journal of Structural Geology*, *4*(1), 69–79. https://doi.org/10.1016/0191-8141(82)90008-6

Passchier, C. W., & Trouw, R. A. J. (2005). *Microtectonics* (2nd ed.). Springer Science & Business Media.

Passelègue, F. X., Tielke, J., Mecklenburgh, J., Violay, M., Deldicque, D., & Di Toro, G. (2021). Experimental plastic reactivation of pseudotachylyte-filled shear zones. *Geophysical Research Letters*, *48*(5), e2020GL091538. https://doi.org/10.1029/2020GL091538

Pennacchioni, G., & Cesare, B. (1997). Ductile-brittle transition in pre-Alpine amphibolite facies mylonites during evolution from water-present to water-deficient conditions (Mont Mary nappe, Italian Western Alps). *Journal of Metamorphic Geology*, *15*(6), 777–791. https://doi.org/10.1111/j.1525-1314.1997.00055.x

Petch, N. J. (1953). The cleavage strength of polycrystals. *Journal of the Iron Steel Institute London*, *174*, 25–28.

Pittarello, L., Levi, N., Wegner, W., & Stehlik, H. (2022). The pseudotachylytes at the base of the Silvretta nappe: A newly discovered recent generation and the tectonomometamophic evolution of the Nappe. *Tectonophysics*, *822*, 229185. https://doi.org/10.1016/j.tecto.2021.229185

Pittarello, L., Pennacchioni, G., & Di Toro, G. (2012). Amphibolite-facies pseudotachylytes in Premosello metagabbro and felsic mylonites (Ivrea Zone, Italy). *Tectonophysics*, *580*, 43–57. https://doi.org/10.1016/j.tecto.2012.08.001

Price, N. A., Johnson, S. E., Gerbi, C. C., & West, D. P. (2012). Identifying deformed pseudotachylyte and its influence on the strength and evolution of a crustal shear zone at the base of the seismogenic zone. *Tectonophysics*, *518–521*, 63–83. https://doi.org/10.1016/j.tecto.2011.11.011

Proctor, B., & Lockner, D. A. (2016). Pseudotachylyte increases the post-slip strength of faults. *Geology*, *44*(12), 1003–1006. https://doi.org/10.1130/G38349.1

Rodgers, C. L., de Cserna, Z., Ojeda Rivera, J., Taverna Amezcua, E., & van Vloten, R. (1962). Tectonic framework of an area within the Sierra Madre Oriental and adjacent Mesa Central, north central Mexico. *Short Papers in Geology and Hydrology: US Geological Survey Professional Paper*, *450*, 21–24.

Röller, K., & Trepmann, C. A. (2003). Stereo32 (Version 1.0.3) [Software]. Ruhr-Universität Bochum. Retrieved from https://data.mendeley.com/datasets/xhh2ktks9g/4

Rowe, C. D., & Griffith, W. A. (2015). Do faults preserve a record of seismic slip: A second opinion. *Journal of Structural Geology*, *78*, 1–26. https://doi.org/10.1016/j.jsg.2015.06.006

Rowe, C. D., Ross, C., Swanson, M. T., Pollock, S., Backeberg, N. R., Barshi, N. A., et al. (2018). Geometric complexity of earthquake rupture surfaces preserved in pseudotachylyte networks. *Journal of Geophysical Research: Solid Earth*, *123*(9), 7998–8015. https://doi.org/10.1029/2018JB016192

Schlische, R. W., Young, S. S., Ackermann, R. V., & Gupta, A. (1996). Geometry and scaling relations of a population of very small rift-related normal faults. *Geology*, *24*(8), 683. https://doi.org/10.1130/0091-7613(1996)024<0683:GASROA>2.3.CO;2

Schmid, S. M., Fügenschuh, B., Kissling, E., & Schuster, R. (2004). Tectonic map and overall architecture of the Alpine orogen. *Eclogae Geolog-icae Helvetiae*, *97*(1), 93–117. https://doi.org/10.1007/s00015-004-1113-x

Schmutz, H.-U. (1995). *Geologische Untersuchungen im SW-Teil des Unterengadiner Fensters: Teil II, Die makroskopische Geometrie der Pseu-dotachylite in der Silvretta-Decke am NW-Rand des Unterengadiner Fensters* (Vol. 166). Baumgartner Druck AG.

Scholz, C. H. (2002). *The mechanics of earthquakes and faulting* (2nd ed.). Cambridge University Press.

Shaw, C. A., & Allen, J. L. (2007). Field rheology and structural evolution of the Homestake shear zone, Colorado. *Rocky Mountain Geology*, *42*(1), 31–56. https://doi.org/10.2113/gsrocky.42.1.31

Sibson, R. H. (1975). Generation of pseudotachylyte by ancient seismic faulting. *Geophysical Journal of the Royal Astronomical Society*, *43*(3), 775–794. https://doi.org/10.1111/j.1365-246X.1975.tb06195.x

Sibson, R. H. (1977). Fault rocks and fault mechanisms. *Journal of the Geological Society*, *133*(3), 191–213. https://doi.org/10.1144/gsjgs.133.3.0191

Sibson, R. H. (1980). Transient discontinuities in ductile shear zones. *Journal of Structural Geology*, *2*(1–2), 165–171. https://doi.org/10.1016/0191-8141(80)90047-4

Stein, R. S., King, G. C. P., & Rundle, J. B. (1988). The growth of geological structures by repeated earthquakes 2. Field examples of continental dip-slip faults. *Journal of Geophysical Research*, *93*(B11), 13319–13331. https://doi.org/10.1029/jb093ib11p13307

Stipp, M., Stünitz, H., Heilbronner, R., & Schmid, S. M. (2002). Dynamic recrystallization of quartz: Correlation between natural and experimental conditions. *Geological Society, London, Special Publications*, *200*(1), 171–190. https://doi.org/10.1144/GSL.SP.2001.200.01.11

Stipp, M., & Tullis, J. (2003). The recrystallized grain size piezometer for quartz. *Geophysical Research Letters*, *30*(21), 1–5. https://doi.org/10.1029/2003GL018444

Stöckhert, B., Brix, M. R., Kleinschrodt, R., Hurford, A. J., & Wirth, R. (1999). Thermochronometry and microstructures of quartz - A comparison with experimental flow laws and predictions on the temperature of the brittle - Plastic transition. *Journal of Structural Geology*, *21*(3), 351–369. https://doi.org/10.1016/S0191-8141(98)00114-X

Swanson, M. T. (1992). Fault structure, wear mechanisms and rupture processes in pseudotachylyte generation. *Tectonophysics*, *204*(3–4), 223–242. https://doi.org/10.1016/0040-1951(92)90309-T

Swanson, M. T. (2006). Late Paleozoic strike-slip faults and related vein arrays of Cape Elizabeth, Maine. *Journal of Structural Geology*, *28*(3), 456–473. https://doi.org/10.1016/j.jsg.2005.12.009

Takagi, H., Goto, K., & Shigematsu, N. (2000). Ultramylonite bands derived from cataclasite and pseudotachylyte in granites, northeast Japan. *Journal of Structural Geology*, *22*(9), 1325–1339. https://doi.org/10.1016/S0191-8141(00)00034-1

Thöni, M. (1981). Degree and evolution of the Alpine metamorphism in the Austroalpine Unit W of the Hohe Tauern in the light of K-Ar and Rb-Sr age determinations on Micas. *Jahrbuch Der Geologischen Bundesanstalt*, *124*, 111–174.

Thöni, M. (1988). Rb-Sr isotopic resetting in mylonites and pseudotachylites: Implications for the detachment and thrusting of the Austroalpine basement nappes in the Eastern Alps. *Jahrbuch Der Geologischen Bundesanstalt*, *131*(1), 169–201.

Trepmann, C. A., Hsu, C., Hentschel, F., Döhler, K., Schneider, C., & Wichmann, V. (2017). Recrystallization of quartz after low-temperature plasticity – The record of stress relaxation below the seismogenic zone. *Journal of Structural Geology*, *95*, 77–92. https://doi.org/10.1016/j.jsg.2016.12.004

Trepmann, C. A., Renner, J., & Druiventak, A. (2013). Experimental deformation and recrystallization of olivine-processes and timescales of damage healing during postseismic relaxation at mantle depths. *Solid Earth*, *4*(2), 423–450. https://doi.org/10.5194/se-4-423-2013

Trepmann, C. A., & Stöckhert, B. (2003). Quartz microstructures developed during non-steady state plastic flow at rapidly decaying stress and strain rate. *Journal of Structural Geology*, *25*(12), 2035–2051. https://doi.org/10.1016/S0191-8141(03)00073-7

Trepmann, C. A., & Stöckhert, B. (2013). Short-wavelength undulatory extinction in quartz recording coseismic deformation in the middle crust - An experimental study. *Solid Earth*, *4*(2), 263–276. https://doi.org/10.5194/se-4-263-2013

Trepmann, C. A., Stöckhert, B., Dorner, D., Moghadam, R. H., Küster, M., & Röller, K. (2007). Simulating coseismic deformation of quartz in the middle crust and fabric evolution during postseismic stress relaxation - An experimental study. *Tectonophysics*, *442*(1–4), 83–104. https://doi.org/10.1016/j.tecto.2007.05.005

Walsh, J. J., & Watterson, J. (1988). Analysis of the relationship between displacements and dimensions of faults. *Journal of Structural Geology*, *10*(3), 239–247. https://doi.org/10.1016/0191-8141(88)90057-0

Wenk, E. (1934). Beiträge zur Petrographie und Geologie des Silvrettakristallins. *Schweizerische Mineralogische Und Petrographische Mitteilungen*, *14*(1), 196–278.

White, J. C. (1996). Transient discontinuities revisited: Pseudotachylyte, plastic instability and the influence of low pore fluid pressure on deformation processes in the mid-crust. *Journal of Structural Geology*, *18*(12), 1471–1477. https://doi.org/10.1016/S0191-8141(96)00059-4

White, J. C. (2004). Instability and localization of deformation in lower crust granulites, Minas fault zone, Nova Scotia, Canada. *Geological Society, London, Special Publications*, *224*(1), 25–37. https://doi.org/10.1144/GSL.SP.2004.224.01.03

White, J. C. (2012). Paradoxical pseudotachylyte - Fault melt outside the seismogenic zone. *Journal of Structural Geology*, *38*, 11–20. https://doi.org/10.1016/j.jsg.2011.11.016

Williams, R. T., & Fagereng, Å. (2022). The role of quartz cementation in the seismic cycle: A critical review. *Reviews of Geophysics*, *60*(1), e2021RG000768. https://doi.org/10.1029/2021RG000768

References From the Supporting Information

Eggleton, R. A. (1972). The crystal structure of stilpnomelane. Part II. The full cell. *Mineralogical Magazine*, *38*(298), 693–711. https://doi.org/10.1180/minmag.1972.038.298.06

Eggleton, R. A., & Chappell, B. W. (1978). The crystal structure of stilpnomelane. Part III: Chemistry and physical properties. *Mineralogical Magazine*, *42*(323), 361–368. https://doi.org/10.1180/minmag.1978.042.323.06

Guggenheim, S., & Eggleton, R. A. (1994). A comparison of the structures and geometric stabilities of stilpnomelane and parsettensite: A distance least-squares (DLS) study. *American Mineralogist*, *79*, 438–442.

Kuebler, K. E. (2013). A combined electron microprobe (EMP) and Raman spectroscopic study of the alteration products in Martian meteorite MIL 03346. *Journal of Geophysical Research: Planets*, *118*(3), 347–368. https://doi.org/10.1029/2012JE004244